Submitted to the Journal of the Atmospheric Sciences

The effects of clouds on the light produced by lightning

L. W. THOMASON AND E. P. KRIDER

Institute of Atmospheric Physics

The University of Arizona, Tucson 85721

18 September 1981

ABSTRACT

A Monte Carlo simulation of the effects of finite clouds on the light impulses produced by point and finite lightning sources within cubical, cylindrical, and spherical clouds shows that absorption is essentially negligible in the visible and near infrared. The fractions of photons which escape various cloud surfaces are given as a function of position and geometry of the source. The light emission is high for intracloud discharges and the in-cloud portion of cloud-to-ground discharges because most lightning activity occurs at the -10 to -30°C temperature level, which, in turn, is usually close to the optical center of the cloud. The characteristic dimensions of the light escaping from a cloud surface are typically 60 to 70% of the cloud dimensions; and the time-broadening of an impulse by multiple scattering can be tens of microseconds or more.

1. Introduction

The optical effects of clouds have been of considerable interest in the atmospheric sciences for many years. Most analytical and numerical solutions of the equation of radiative transfer have been obtained for situations where there are plane parallel sources of radiation incident on infinite homogeneous cloud layers. To the best of our knowledge, no computations have yet been published which describe the transport of radiation produced by a transient and finite light source, such as lightning, which is located within finite clouds.

Understanding the effects of clouds on lightning signals is important because optical sensors have been or are currently being used to detect and locate discharges from ground-based stations (Kitagawa and Kobayashi, 1959; Brook and Kitagawa, 1960; Krider, 1966; Clegg, 1971; Mackerras, 1973; Kidder, 1973; Griffiths and Vonnegut, 1975), from aircraft (Vonnegut and Passarelli, 1978; Brook *et al.*, 1980), and from satellites (Sparrow and Ney, 1968; Vorphal *et al.*, 1970; Turman, 1977, 1978, 1979; Edgar, 1978, 1980; Orville and Spencer, 1979; Turman and Tettelbach, 1980; Orville, 1981; Turman and Edgar, 1981). Clouds obviously affect the amplitudes of the light signals and the apparent dimensions of the optical source; and the multiple scattering alters the shapes of the light signals vs. time.

Here we briefly describe a Monte Carlo computer simulation of the transport of visible and near-infrared light within a cloud. We give results of tests of the program and then calculate the cloud transmission and absorption, the positions and angular distributions of photons which escape the cloud, and the time-broadening of pulses by multiple scattering. These calculations are done for point sources at various

locations within cubical, spherical, and cylindrical clouds; and the effects with finite channels are computed using symmetry and superposition.

2. The Monte Carlo method

The optical characteristics of clouds are described in works by Twomey *et al.* (1967), Rozenberg (1968), Danielson *et al.* (1969), Twomey (1971, 1977), Hansen and Travis (1974), van de Hulst (1980), and many others. Since the radius, a, of a typical cloud drop is large compared to the wavelength, λ, of visible light, the size parameter, $2\pi a/\lambda$, is large and the scattering and absorption by the drops is described by the Mie equations (van de Hulst, 1957). Following Danielson *et al.* (1969) and others, we approximate the angular distribution of the photons which are scattered by a cloud drop by the Henyey-Greenstein phase function:

$$p(\mu) = \frac{1 - g^2}{(1 + g^2 - 2g\mu)^{3/2}} \qquad (1)$$

where μ is the cosine of the scattering angle measured in the scattering plane, and g, the asymmetry factor, is the intensity-weighted mean of μ over all angles. The scattering is assumed to be symmetric about the direction of the incident photon. The probability that a photon is absorbed during a scattering event is described by the single-scattering albedo, $\bar{\omega}_0$. $\bar{\omega}_0$ equals unity for conservative scattering, and $(1 - \bar{\omega}_0)$ is the probability that a photon is absorbed per scattering event.

Basically, our Monte Carlo simulation approximates the physical interactions between individual photons and the cloud drops, and is similar to the methods described by Plass and Kattawar (1968), Danielson *et al.* (1969), Van Blerkom (1971), Bucher (1973), McKee and Cox (1974), Davis *et al.* (1976), Aida (1977), Davies (1978), and others. Photons are emitted isotropically from a point source, travel a certain distance, and then interact with a

cloud drop at a known position within the cloud. During the interaction, photons are either absorbed with a probability of $(1 - \bar{\omega}_0)$ or scattered with the angular distribution given by Eq. (1). This process continues until the photon either is absorbed or escapes from the cloud surface. Here we consider only interactions with the cloud particles, and we ignore any molecular absorption or scattering, either inside or outside the cloud.

To derive the free paths of photons between interactions, we assume that the probability that a photon travels a distance x without an interaction is

$$P(x) = e^{-x/\Lambda} \tag{2}$$

where Λ is the mean free path. If we choose a random number, r, between 0 and 1, a free path is given by

$$x = -\Lambda \ell n(r) \ . \tag{3}$$

To save on computing time, the scattering angles were selected at random from an array of size N, where each angle entry had equal probability. These angles were computed using Eq. (1); that is,

$$\frac{1}{N} = \int_{\mu_{n-1}}^{\mu_n} \frac{(1 - g^2)\, d\mu}{(1 + g^2 - 2g\mu)^{3/2}} \tag{4}$$

or

$$\mu_n = \frac{(1 + g^2) - \left[\frac{g}{N(1 - g^2)} + (1 + g^2 - 2g\mu_{n-1})^{-\frac{1}{2}}\right]}{2g} \ , \tag{5}$$

so that the nth scattering angle, $\theta(n)$ is given by

$$\theta(n) = \cos^{-1}\left[(\mu_n + \mu_{n-1})/2\right] \ . \tag{6}$$

For our application, N was typically 2000. When a photon escaped from the cloud surface, its position, direction, and total path length were stored in an array for subsequent output.

3. Cloud models

For large size parameters, the extinction efficiency of a spherical drop is approximately 2 (van de Hulst, 1957); and the interaction mean free path of photons with a uniform population of drops is approximately:

$$\Lambda \simeq \frac{1}{2\pi a^2 N} , \tag{7}$$

where a is the mean radius, and N is the number density of drops. The total optical depth, τ, of a uniform cloud layer of geometric thickness L is

$$\tau = \frac{L}{\Lambda} . \tag{8}$$

Table 1 shows values of mean drop radii and number densities for a cloud with a liquid-water content of 0.42 gm/m^3. The associated photon mean free paths and the geometrical dimensions corresponding to total optical depths of 80, 200, and 400 are also shown. The 5 μm radius drops in Table 1 correspond to a typical continental cloud, and the larger radii correspond to maritime clouds. In the following, we will give the results of our calculations for a specific optical depth, and Eqs. (7) and (8) can be used to relate these data to the particular type of cloud.

TABLE 1. Geometric parameters.

Mean Radius a (μm)	Number Density N (cm^{-3})	Mean Free Path Λ (m)	Dimension, L (km)		
			τ = 80	τ = 200	τ = 400
5	800	8	0.64	1.6	3.2
10	100	16	1.3	3.2	6.4
15	30	24	1.9	4.8	9.6

Table 2 gives values of the single-scattering albedo and asymmetry factor for water and ice spheres in the visible (0.45 μm) and near-infrared (0.87 μm) regions of the spectrum. The $\bar{\omega}_0$ values for water drops were calculated from Mie theory using the refractive index data of Hale and Querry (1973). The $\bar{\omega}_0$ values for ice particles at .87 μm were approximated using the refractive index data of Irvine and Pollack (1968) at 0.95 μm, assuming the particles are spherical. Note that the single-scattering albedos of both water and ice in the visible, where there are many emission lines in the lightning spectrum (Salanave, 1980), are essentially unity; therefore, the scattering in this region is conservative. The $\bar{\omega}_0$ values in the near-infrared, a region where there is strong NI radiation in the lightning spectrum and where silicon optical detectors have optimum spectral response (Wolfe and Zissis, 1978), range from 0.9983 to 0.99997, all nearly conservative. The calculations which will be discussed below were performed for $\bar{\omega}_0$ values of 0.99990, 0.99996, and 1.0000 with 0.99996 being regarded as typical.

TABLE 2. Optical parameters.

Spectral Region	Radius a (μm)	Water		Ice	
		$\bar{\omega}_0$	g	$\bar{\omega}_0$	g
Visible (0.45 μm)	5	1.0000	0.85	1.0000	0.85
	10	1.0000	0.87	1.0000	0.87
	15	1.0000	0.88	1.0000	0.88
Near IR (0.87 μm)	5	0.99997	0.81	0.99992	0.82
	10	0.99996	0.84	0.99990	0.87
	15	0.99995	0.87	0.99983	0.87

The asymmetry factors in Table 2 were taken from Hansen and Travis (1974), who assumed the particle size distribution discussed by Hansen (1971). The

values range from 0.81 to 0.88, and, in the following, we assume 0.84 is typical. Since we will be concerned only with clouds that have rather large optical depths, we can use the scaling or similarity principles discussed by van de Hulst and Grossman (1968), Twomey and Bohren (1980), and van de Hulst (1980, Ch. 14) to apply our results to other cases. That is, the results for a given $\bar{\omega}_0$, g, and τ can be applied to a situation where there are other values, $\bar{\omega}_0'$, g', and τ', provided that

$$\bar{\omega}_0\tau(1 - g) = \bar{\omega}_0'\tau'(1 - g') \tag{9}$$

and

$$(1 - \bar{\omega}_0)\tau = (1 - \bar{\omega}_0')\tau' . \tag{10}$$

Recent work on the locations of lightning discharge channels and the electric charges inside thunderclouds suggests that most lightning activity is confined to a rather narrow vertical region of the cloud near the -10°C to -20°C temperature level (Teer and Few, 1974; Jacobson and Krider, 1976; Taylor, 1978; Krehbiel *et al.*, 1979; and Proctor, 1981). The -10 to -20°C level, in turn, is usually located just about halfway between cloud base and cloud top in both continental and maritime storms (see, for example, Byers and Braham, 1949, and Magono, 1980). In the following, we assume that the light impulses which are produced by the individual components of an intracloud discharge, or the in-cloud portion of a cloud-to-ground flash, are isotropic point sources located on or near the horizontal mid-plane of the cloud. The effects of an extended channel geometry, either in the mid-plane or with large vertical components, can be derived from these results, using the symmetry of the cloud and the principle of superposition.

4. Program verification

The two main limitations of the Monte Carlo method are the limited number of photons which can be traced through an optically thick cloud with finite

computer time, and the fact that a Monte Carlo program cannot be formally proven to be mathematically correct for a finite number of photons. Here, we choose a sufficient number of photons to keep most of our numerical values accurate to at least 5%; and we verify the program by comparing certain specific calculations with previous analytical and Monte Carlo results. In the computations to be presented below, the standard deviation of a particular numerical value is determined using the binomial distribution. That is, if the fraction of photons contributing to a particular result is p, and if the total number of photons is n, then the standard deviation is given by

$$\sigma = \left[\frac{p(1 - p)}{n}\right]^{\frac{1}{2}} . \tag{11}$$

Verification of the Monte Carlo results can be obtained by computing the optical properties of semi-infinite cloud layers with external illumination. Following Chandrasekhar (1950) and Twomey and Bohren (1980), the fractional absorption, α, of a layer of isotropic scatterers can be expressed by

$$\alpha = (1 - \bar{\omega}_0)^{\frac{1}{2}} H(\mu_0) \tag{12}$$

where $H(\mu_0)$ is the H-function as defined by Chandrasekhar (1950) and μ_0 is the cosine of the angle of incidence. Twomey and Bohren (1980) show that this relation also approximates anisotropic scattering ($g' \neq 0$) if $\bar{\omega}_0$ is replaced by a scaled single-scattering albedo derived from Eqs. (9) and (10)

$$\bar{\omega}_0 = \frac{(1 - g')\,\bar{\omega}_0'}{1 - g'\,\bar{\omega}_0'} \tag{13}$$

so that Eq. (11) becomes

$$\alpha \approx \left[\frac{1 - \bar{\omega}_0'}{1 - g'\,\bar{\omega}_0'}\right] H(\mu_0) \tag{14}$$

Figure 1 shows a plot of layer absorption vs. $\bar{\omega}_0$ computed using Eq. (14) and our Monte Carlo results for a g' of 0.84. The agreement is quite good.

Figure 2 shows Monte Carlo calculations of the reflectance of conservative scattering layers ($\bar{\omega}_0 = 1$) with the optical depths and asymmetry factors as shown. The τ and g values were chosen so that the scaled optical thickness for conservative symmetric scattering ($g' = 0$), which is derived from Eq. (9)

$$\tau_s = (1 - g)\tau \ , \tag{15}$$

equals 6 in Fig. 2a and equals 12 in Fig. 2b. Note that the Monte Carlo results preserve the scaling relation given by Eq. (15).

Twomey *et al.* (1967) used a matrix method to derive the mean optical path length of reflected and transmitted photons vs. optical thickness for layer clouds. Figure 3 shows a plot of these values together with our Monte Carlo results, and the agreement is quite good.

McKee and Cox (1974) used a Monte Carlo program to calculate the reflectance of both layer and cubical clouds with conservative scattering. Figure 4 shows the McKee and Cox values for different optical depths, together with those provided by our program; and again, the agreement is good.

5. Results

For this study, we have computed the optical effects of cubical, spherical, and cylindrical clouds with total optical depths of 80, 200, and 400. These computations were done for a series of point sources at the locations shown in Fig. 5. For the cube, the coordinates of the source points are labeled in a scaled Cartesian coordinate system (x,y,z) centered on one corner and with unity the length of each side. The center of the cube, for example, is the point (0.5, 0.5, 0.5). If the cube had a total optical depth of 200, the center is (100, 100, 100) in optical depth units; or, if we consider the cloud with 10 μm radius drops in Table 1, the center would be (1.6, 1.6, 1.6) in kilometers.

Point sources within the sphere of scaled diameter unity are taken along a fixed radius, starting at the center (0.5, 0.5, 0.5) and moving outward almost to the outer surface (0.99, .5, .5). The cylinder has a scaled height and diameter of unity. Point sources within the cylinder are labeled in (x,y,z) coordinates with the center at 0.5, 0.5, 0.5).

In order to describe the photons which escape from the cloud surface, it will be convenient to number the faces of the cube as shown in Fig. 5a. For the sphere, 6 output surfaces of equal area are defined and labeled as shown in Fig. 5b. For the cylinder, the vertical surface is divided into 4 equal sections by the $x = y$ and $x = -y$ planes, and all surfaces are labeled as shown in Fig. 5c.

The results of Monte Carlo calculations of the total cloud absorption and the fraction of photons which escape from the various cloud surfaces are summarized in the Appendix, Tables A-1, A-2, and A-3, for the point sources sketched in Fig. 5. The total absorption is simply the fraction of source photons which is absorbed by the cloud. The escape percentages are the fractions of source photons which escape through the specified surfaces; the sum of the total absorption and the 6 escape fractions should equal 100%.

The point sources sketched in Fig. 5 model localized discharge components, such as K-changes or channel sections, which make up the in-cloud portion of both cloud-to-ground and intracloud lightning (Kitagawa and Kobayashi, 1959; Kitagawa and Brook, 1960; Uman, 1969; and Brook and Ogawa, 1977). The effects of clouds on extended channels can be derived from the results in Tables A-1, A-2, and A-3, using symmetry and superposition. Figure 6 shows sketches of the geometry of several extended sources that were computed using the cubical cloud model; the associated optical results are given in Table 3. The structures in Fig. 6 lie on the horizontal mid-plane; however, because

TABLE 3. Computations of photon absorption and escape for a cubical cloud with the finite source channels shown in Fig. 6. All computations were done for $g = 0.84$.

Source Structure	Faces	Escape in % per Cloud Face	Faces	Escape in % per Cloud Face	Total Absorption in % α	Optical Parameters	
						ω_0	τ
A	1,2,3,4	19.0 ± 1.0	5,6	11.6 ± 0.8	0.8 ± 0.2	0.99996	80
A		18.2 ± 0.7		9.5 ± 0.5	8.5 ± 0.5	0.99990	200
A		18.8 ± 0.7		10.7 ± 0.5	3.6 ± 0.3	0.99996	
A		19.5 ± 0.7		11.2 ± 0.5	0	1.00000	
A		17.9 ± 0.6		8.8 ± 0.5	11.1 ± 0.5	0.99996	400
A‡	1,2,3,4	17.0 ± 1.0	5,6	15.1 ± 0.9	1.1 ± 0.3	0.99996	80
A‡		15.5 ± 0.6		13.7 ± 0.5	10.6 ± 0.5	0.99990	200
A‡		16.6 ± 0.6		14.4 ± 0.6	4.6 ± 0.4	0.99996	
A‡		17.4 ± 0.6		15.2 ± 0.6	0	1.00000	
A‡		15.0 ± 0.6		12.3 ± 0.5	15.6 ± 0.6	0.99996	400
B	1,2,3,4	20.3 ± 0.7	5,6	8.1 ± 0.5	2.7 ± 0.3	0.99996	200
B‡		17.7 ± 1.0		12.5 ± 0.9	4.2 ± 0.5	0.99996	
C	1,2	26.4 ± 1.1	3,4,5,6	11.6 ± 0.6	0.8 ± 0.2	0.99996	80
C		26.7 ± 0.7		9.5 ± 0.5	8.5 ± 0.5	0.99990	200
C		26.8 ± 0.7		10.7 ± 0.5	3.6 ± 0.3	0.99996	
C		27.7 ± 0.8		11.2 ± 0.5	0	1.00000	
C		27.1 ± 0.8		8.8 ± 0.5	11.1 ± 0.5	0.99996	400
C‡	1,2	19.0 ± 1.0	3,4,5,6	15.1 ± 0.9	1.1 ± 0.3	0.99996	80
C‡		17.4 ± 0.6		13.7 ± 0.5	10.6 ± 0.5	0.99990	200
C‡		18.8 ± 0.7		14.4 ± 0.6	4.6 ± 0.4	0.99996	
C‡		19.6 ± 0.7		15.2 ± 0.6	0	1.00000	
C‡		17.7 ± 0.6		12.3 ± 0.5	15.6 ± 0.6	0.99996	400
D	1,2,3,4	20.3 ± 0.7	5,6	8.1 ± 0.5	2.7 ± 0.3	0.99996	200
D‡		17.7 ± 1.0		12.5 ± 0.9	4.2 ± 0.5	0.99996	

of the symmetry, the results for vertical channels can be determined simply by relabeling the output faces. Among the things to note in Table 3 are the comparatively small values of total absorption, even for clouds with an optical thickness of 400. This is because the single-scattering albedos in Table 2 are all close to unity; therefore, even under extreme circumstances, the visible and near-infrared light escaping from the cloud will always be a sizable fraction of the total light emitted by the discharge. Figure 7 shows the total absorption vs. point source position for a nonconservative cubical cloud with optical depths of 200 and 400. Total absorption is the greatest for point sources near the center of the cloud (also see Tables A-1, A-2, and A-3) because of the exponential behavior of the scattering process.

Since absorption is essentially negligible, the primary optical effects of clouds are a redistribution of the numbers and directions of photons which escape the various surfaces and the time-broadening of the pulses due to multiple scattering. The fractions of photons which escape face 2 in the cubical cloud are plotted in Fig. 8 as a function of source position, single-scattering albedo, and optical depth. The nearly exponential increase of the escape fraction as the source approaches the surface is not affected by changes in the single-scattering albedo. An increase in the absorption or optical depth merely tends to lower the entire curve. It should be noted that, with the source essentially at the surface of face 2 (0.99, 0.5, 0.5) and a τ of 200, almost 93% of the photons escape from that face and only about 0.3% escape from the opposite surface (face 1). The escape from face 1 for other source positions can be obtained simply by relabeling the x-axis in Fig. 8 to be from 1.0 to 0 rather than from 0 to 1.0. The data for escape as a function of source position along the $x = y$ diagonal ($z = 0.5$) are also plotted in Fig. 8.

For the sources plotted in Fig. 8 along the (x, 0.5, 0.5) axis, faces 1 and 2 are normal to the source axis. Faces 3, 4, 5, and 6 are parallel to this axis. Figure 9 shows the sum of the fractions of photons which escape through the parallel faces when the source moves along the (x, 0.5, 0.5) axis. The curves are symmetric about $x = 0.5$; and, again, the effect of increasing absorption or optical depth is to simply lower the entire curve.

One of the greatest difficulties with the Monte Carlo method is in obtaining reliable statistics for the angular distributions of the escaping photons because of the large number of "boxes" into which the photon angles are divided. Fortunately, the nature of the statistical error is such that it is smallest where the frequency of emission is largest [see Eq. (11)]. Figure 10 shows the zenith angle distribution of photons which escape through parallel faces 5 and 6 (the bottom and top, respectively). Half of the escaping photons emerge within about 45 degrees of the vertical axis [$|\cos(Z)| \geq .7$], and the zenith-angle distributions are essentially independent of the source position and total optical depth. The distribution of azimuth angles of the photons which escape from faces 5 and 6 with the source positions of Fig. 10 are essentially isotropic.

Figures 11 and 12 show the zenith and azimuth angle distributions for photons which escape from faces 1, 2, 3, and 4. The solid curves in Figures 10, 11 and 12 have actually been drawn to provide the best fit to the means of the angular distributions derived from all point-source locations that are at least 0.25 scaled-distance units away from the surface.

The enhancement of photon optical paths within the cloud by multiple scattering will cause a time broadening of an impulsive light signal. To determine the magnitude of this effect, Figures 13 and 14 show distributions of the optical paths of all photons which escape from the cloud surface in

units of the mean free path (Eq. 7). If the point source is a delta function with time, these curves show the time broadening when the optical path is converted to geometric units and divided by the speed of light. That is, each unit of optical path corresponds to a time interval given by

$$t_\Lambda = \Lambda/c \tag{16}$$

where Λ is given by Eq. (7) and c is the speed of light. Since Λ for the 10 μm radius drops in Table I is 16 m, t_Λ in this case would be about 53 nanoseconds per optical path unit.

Figure 15 shows the mean and the most probable optical paths that were computed for photons which escape the cubical cloud as a function of the point-source location along the (x, 0.5, 0.5) axis. It should be noted in Figs. 13, 14, and 15 that the time-broadening is largest when the sources are near the middle of the cloud and when the optical depths are large. For a point source at the center (0.5, 0.5, 0.5), the mean optical paths of photons reaching the surface would be 970 and 2790 for cloud depths of 200 and 400, respectively. For the 10 μm radius drops in Table I, these mean optical paths would correspond to mean time-delays of 51 and 148 microseconds, respectively. It should be noted that the curves in Fig. 15 will be symmetric about the x = 0.5 position.

The number of photons which escape a unit area of cloud surface is a function of position on the surface. In order to describe this function for the different faces of our cubical cloud, we will consider the dimension, S, of a hypothetical square centered on each face and examine the fraction of photons emitted from within its boundaries. For the spherical cloud, we imagine a surface bounded by a circle of diameter, S, on the hemisphere containing the source and determine the fraction of the photons which escape

this surface. A point source at the center of the sphere produces a uniform illumination of the entire surface. Figure 16 shows the fractions of photons which escape from surface 2 of the cube and the source hemisphere as a function of the characteristic distance, S, for various point sources within cubical and spherical clouds. All curves lie between the cases where there is uniform illumination (curve 9) and the image of a point source on the surface (curves 1 and 2).

If we define a characteristic dimension of the emission from a surface, S_0, to be that value of S which contains 70% of the photons emitted from the face of a cube, or, in the case of a spherical cloud, the S which contains 70% of the photons which escape from the hemisphere containing the source, then we can plot S_0 as a function of the source position as shown in Fig. 17. Note that the characteristic dimensions of the surface illumination are all about 0.6 to 0.7 scale units when the sources are deeper than about 0.2 from the surface. It should also be noted that the characteristic dimension seems to be inversely proportional to the fraction of photons which escape through the surface (see Table A-1).

If the cloud is observed from a large distance, such as from a satellite, the number of photons which escape from the cloud as a whole determine the brightness of the source. In this case, each face of the cube can be approximated by a point source emitting the fraction of photons listed in Table A-1, with the angular distributions plotted in Figs. 10, 11, and 12. The fraction of photons, P_f, passing through a certain solid angle, $\Delta\omega_i$ is obtained by summing over the visible faces,

$$P_f = \sum_n F_n \, \Delta\omega_i \tag{17}$$

where $F_n(\Delta\omega_i)$ is the fraction of photons emitted from face n through $\Delta\omega_i$.

$F_n(\Delta\omega_i)$ can be expressed as $F_n \cdot \theta_n(\mu_i) \cdot \phi(\phi_i)$, where F_n is the fraction of source photons emitted from face n, $\phi(\mu_i)$ is the fraction of photons emitted from face n with $\mu_i = \cos\theta_i$ between $\mu_i - \frac{1}{2}\Delta\mu$ and $\mu_i + \frac{1}{2}\Delta\mu$ and $\phi_n(\phi_i)$ is the fraction of photons emitted from face n with ϕ between $\phi_i - \frac{1}{2}\Delta\phi$ and $\phi_i + \frac{1}{2}\Delta\phi$. Here we let $\Delta\mu = .1$ and $\Delta\phi = .1\pi$, so there are 400 solid-angle elements each of $.01\pi$ steradians.

Figures 18 and 19 give the fractions of source photons which would be detected in the $y = 0.5$ plane as a function of the zenith angle, Z, measured from the positive z-axis and moving initially toward the positive x-axis. Note that there is a uniform brightness with angle when the source is in the center of either the cube or the sphere. The light intensity changes very rapidly with angle when Z is near 0 or π with both cubical and spherical geometries.

Figure 20 shows the angular distributions of source brightness with several extended channel sources, as sketched in Fig. 6. Note in Fig. 20 how the effects of a large source geometry tend to eliminate the rapid intensity variations with angle. If the zenith angle, Z, is defined so that it moves toward the positive y-axis, rather than the x-axis, the brightness distributions for the sources plotted in Figs. 18, 19, and 20 are uniform with angle.

6. Discussion

In order to perform the above calculations, we have been forced to make several simplifying assumptions about the geometry and composition of thunderstorm clouds and the nature of lightning sources. Spheres, cubes, and cylinders, of course, do not exhibit the ebullient irregularities of natural clouds. A homogeneous composition virtually ignores any possible differences in the optical characteristics of water and ice particles and possible variations in drop concentrations and mean radii within the cloud. The

Henyey-Greenstein phase function is a good approximation for most drop-size distributions, but it is not exact. In spite of these difficulties, however, we expect the basic aspects and trends of most of our results to be valid.

By modeling lightning as a series of point sources within the cloud, we obviously ignore any contributions which would arise from channels outside the cloud surface. Light from a cloud-to-ground channel, for example, could reach an optical detector directly or by reflections from (or transmissions through) cloud surfaces. In Fig. 2 and Table 3, we see that the main effect of even a thin cloud layer on the light produced by a source outside the surface is reflection. Table 3 also shows that the transmission through even a small cloud ($\tau = 80$) is limited to just a few percent of the source or less.

We will now summarize our results by considering the problem of detecting lightning from an earth-orbiting satellite with an optical sensor. The high reflectivity of even thin cloud layers will prevent almost all the light produced below or behind a cloud from reaching the detector; therefore, we can expect a very poor detection efficiency on most cloud-to-ground channels. This situation might be alleviated somewhat by reflections of light from the ground or other clouds, but, in these cases, the location accuracy will be poor.

As we have said before, most lightning activity occurs within the cloud at altitudes which are close to the optical center. Most cloud-to-ground flashes are initiated inside the cloud at these same altitudes and have extensive in-cloud components. Since the effects of absorption tend to be negligible, any channels or portions of channels which are symmetric about the center of the cloud will produce time-integrated signals which are essentially the same as if there were no cloud present at all. If the

channels are above the geometrical midplane, the effects of the cloud will be to enhance the signal detected by the satellite, and sources below the midplane will be reduced in intensity quite rapidly with distance. Absolute measurements of the source intenstiy will not be possible unless the locations of the channels inside the cloud are known with good accuracy. For deep sources, the characteristic dimensions of the light escaping the cloud will be roughly 60 to 70% of the cloud dimensions; and if the channels are extensive, the intensity will be substantially independent of direction.

The risetimes of lightning light signals are probably dominated by the geometrical growth of the channels which produce the emissions (Krider, 1966). Short channels can produce fast risetimes (Krider, 1974), but our calculations suggest that these risetimes cannot be measured outside the cloud because the time-broadening due to multiple scattering can easily be several tens of microseconds.

Acknowledgments. The authors are very grateful to Prof. S. Twomey at The University of Arizona for numerous helpful discussions and to Prof. C. Bohren at The Pennsylvania State University for comments on the manuscript. This research has been submitted in partial fulfillment of the requirements for an M.S. degree at The University of Arizona by one of the authors (L.W.T.). The work has been supported in part by the NASA Marshall Space Flight Center, Contract NAS8-33718, and the Office of Naval Research, Contract N00014-81-K-0175.

APPENDIX

TABLE A-1. Computations of photon absorption and escape for cubical clouds.

Point Source Location (x,y,z)	Percent Escape Through Cloud Face						Total Absorption in %	Optical Parameters		
	1	2	3	4	5	6	a	ω_0	g	τ
.50,.50,.50	16.4 ± 0.9	16.4 ± 0.9	16.4 ± 0.9	16.4 ± 0.9	16.4 ± 0.9	16.4 ± 0.9	1.3 ± 0.2	0.99996	0.84	80
.65,.50,.50	8.7 ± 0.7	30.7 ± 1.2	14.9 ± 0.9	14.9 ± 0.9	14.9 ± 0.9	14.9 ± 0.9	1.1 ± 0.3			
.75,.50,.50	6.2 ± 0.6	39.1 ± 1.3	13.4 ± 0.9	13.4 ± 0.9	13.4 ± 0.9	13.4 ± 0.9	1.0 ± 0.3			
.85,.50,.50	3.4 ± 0.5	57.5 ± 1.3	9.7 ± 0.8	9.7 ± 0.8	9.7 ± 0.8	9.7 ± 0.8	0.3 ± 0.1			
.99,.50,.50	1.3 ± 0.3	86.3 ± 0.9	3.0 ± 0.4	3.0 ± 0.4	3.0 ± 0.4	3.0 ± 0.4	0.3 ± 0.1			
.75,.50,.50	6.3 ± 0.6	37.5 ± 1.2	13.8 ± 0.9	13.8 ± 0.9	13.8 ± 0.9	13.8 ± 0.9	0.9 ± 0.2	0.99996	0.884	80
.75,.50,.50	5.5 ± 0.6	41.7 ± 1.3	12.9 ± 0.9	12.9 ± 0.9	12.9 ± 0.9	12.9 ± 0.9	1.1 ± 0.3		0.800	
.75,.50,.50	5.1 ± 0.6	43.3 ± 1.3	12.6 ± 0.9	12.6 ± 0.9	12.6 ± 0.9	12.6 ± 0.9	1.1 ± 0.3		0.750	
.50,.50,.50	15.2 ± 0.5	15.2 ± 0.5	15.2 ± 0.5	15.2 ± 0.5	15.2 ± 0.5	15.2 ± 0.5	8.7 ± 0.4	0.99990	0.87	200
.50,.50,.50	14.8 ± 0.5	14.8 ± 0.5	14.8 ± 0.5	14.8 ± 0.5	14.8 ± 0.5	14.8 ± 0.5	11.3 ± 0.4	0.99990	0.84	200
.65,.50,.50	6.3 ± 0.7	27.3 ± 1.4	13.9 ± 1.1	13.9 ± 1.1	13.9 ± 1.1	13.9 ± 1.1	10.7 ± 0.9			
.75,.50,.50	4.1 ± 0.3	43.7 ± 0.7	10.7 ± 0.4	10.7 ± 0.4	10.7 ± 0.4	10.7 ± 0.4	9.5 ± 0.4			
.85,.50,.50	2.4 ± 0.5	55.9 ± 1.6	8.7 ± 0.9	8.7 ± 0.9	8.7 ± 0.9	8.7 ± 0.9	7.1 ± 0.8			
.99,.50,.50	0.4 ± 0.1	92.7 ± 0.4	1.3 ± 0.2	1.3 ± 0.2	1.3 ± 0.2	1.3 ± 0.2	1.6 ± 0.2			
.50,.50,.50	15.8 ± 0.5	15.8 ± 0.5	15.8 ± 0.5	15.8 ± 0.5	15.8 ± 0.5	15.8 ± 0.5	5.3 ± 0.3	0.99996	0.84	200
.65,.50,.50	7.9 ± 0.8	29.5 ± 1.4	14.5 ± 1.1	14.5 ± 1.1	14.5 ± 1.1	14.5 ± 1.1	4.5 ± 0.7			
.75,.50,.50	4.3 ± 0.3	44.2 ± 0.7	11.9 ± 0.5	11.9 ± 0.5	11.9 ± 0.5	11.9 ± 0.5	3.8 ± 0.3			
.85,.50,.50	3.1 ± 0.5	60.3 ± 1.5	8.1 ± 0.9	8.1 ± 0.9	8.1 ± 0.9	8.1 ± 0.9	3.1 ± 0.5			
.95,.50,.50	0.8 ± 0.1	82.1 ± 1.0	3.7 ± 0.5	3.7 ± 0.5	3.7 ± 0.5	3.7 ± 0.5	2.3 ± 0.4			
.99,.50,.50	0.3 ± 0.1	92.8 ± 0.4	1.6 ± 0.2	1.6 ± 0.2	1.6 ± 0.2	1.6 ± 0.2	0.7 ± 0.1			
.65,.65,.50	7.9 ± 0.7	28.0 ± 1.2	7.9 ± 0.7	28.0 ± 1.2	12.1 ± 0.8	12.1 ± 0.8	4.0 ± 0.5	0.99996	0.84	200
.75,.75,.50	3.1 ± 0.2	37.0 ± 0.7	3.1 ± 0.2	37.0 ± 0.7	8.5 ± 0.4	8.5 ± 0.4	2.8 ± 0.2			
.85,.85,.50	1.5 ± 0.3	43.4 ± 1.3	1.5 ± 0.3	43.4 ± 1.3	4.0 ± 0.5	4.0 ± 0.5	2.3 ± 0.4			
.99,.99,.50	———	49.8 ± 0.7	———	49.8 ± 0.7	0.1 ± 0.1	0.1 ± 0.1	0.1 ± 0.1			
.65,.65,.65	6.7 ± 0.6	25.4 ± 1.1	6.7 ± 0.6	25.4 ± 1.1	6.7 ± 0.6	25.4 ± 1.1	3.7 ± 0.5	0.99996	0.84	200
.75,.75,.75	2.9 ± 0.4	29.5 ± 1.2	2.9 ± 0.4	29.5 ± 1.2	2.9 ± 0.4	29.5 ± 1.2	3.0 ± 0.4			
.85,.85,.85	0.7 ± 0.2	32.1 ± 1.2	0.7 ± 0.2	32.1 ± 1.2	0.7 ± 0.2	32.1 ± 1.2	1.5 ± 0.3			
.99,.99,.99	———	33.3 ± 1.2	———	33.3 ± 1.2	———	33.3 ± 1.2	0.1 ± 0.1			
.50,.50,.50	16.7 ± 0.9	16.7 ± 0.9	16.7 ± 0.9	16.7 ± 0.9	16.7 ± 0.9	16.7 ± 0.9	0	1.00000	0.84	200
.65,.50,.50	8.1 ± 0.7	31.4 ± 1.2	15.1 ± 0.9	15.1 ± 0.9	15.1 ± 0.9	15.1 ± 0.9	0			
.75,.50,.50	5.4 ± 0.6	43.3 ± 1.3	12.8 ± 0.9	12.8 ± 0.9	12.8 ± 0.9	12.8 ± 0.9	0			
.85,.50,.50	2.0 ± 0.4	65.3 ± 1.2	8.2 ± 0.7	8.2 ± 0.7	8.2 ± 0.7	8.2 ± 0.7	0			
.99,.50,.50	0.3 ± 0.1	93.1 ± 0.7	1.7 ± 0.3	1.7 ± 0.3	1.7 ± 0.3	1.7 ± 0.3	0			
.50,.50,.50	13.8 ± 0.5	13.8 ± 0.5	13.8 ± 0.5	13.8 ± 0.5	13.8 ± 0.5	13.8 ± 0.5	17.4 ± 0.5	0.99996	0.84	400
.65,.50,.50	6.2 ± 0.6	28.9 ± 1.2	12.9 ± 0.9	12.9 ± 0.9	12.9 ± 0.9	12.9 ± 0.9	13.5 ± 0.9			
.75,.50,.50	3.1 ± 0.2	44.3 ± 0.7	10.0 ± 0.4	10.0 ± 0.4	10.0 ± 0.4	10.0 ± 0.4	12.7 ± 0.5			
.85,.50,.50	2.0 ± 0.4	61.0 ± 1.3	7.0 ± 0.7	7.0 ± 0.7	7.0 ± 0.7	7.0 ± 0.7	9.1 ± 0.7			
.95,.50,.50	0.3 ± 0.1	93.1 ± 0.4	2.6 ± 0.2	2.6 ± 0.2	2.6 ± 0.2	2.6 ± 0.2	3.6 ± 0.3			
.99,.50,.50	0.2 ± 0.1	93.8 ± 0.4	1.0 ± 0.3	1.0 ± 0.3	1.0 ± 0.3	1.0 ± 0.3	1.9 ± 0.4			

TABLE A-2. Computations of photon absorption and escape for a spherical cloud.

Point Source Location (x,y,z)	Percent Escape Through Cloud Face						Total Absorption in % α	Optical Parameters		
	1	2	3	4	5	6		ω_0	g	τ
.50,.50,.50	16.1 ± 0.5	16.1 ± 0.5	16.1 ± 0.5	16.1 ± 0.5	16.1 ± 0.5	16.1 ± 0.5	3.4 ± 0.3	0.99996	0.84	200
.65,.50,.50	7.2 ± 0.4	31.9 ± 0.7	14.5 ± 0.5	14.5 ± 0.5	14.5 ± 0.5	14.5 ± 0.5	3.1 ± 0.2			
.75,.50,.50	4.2 ± 0.3	47.8 ± 0.7	11.3 ± 0.4	11.3 ± 0.4	11.3 ± 0.4	11.3 ± 0.4	2.8 ± 0.2			
.85,.50,.50	2.0 ± 0.2	69.5 ± 0.7	6.6 ± 0.4	6.6 ± 0.4	6.6 ± 0.4	6.6 ± 0.4	2.1 ± 0.2			
.99,.50,.50	0.8 ± 0.2	95.3 ± 0.7	0.9 ± 0.2	0.9 ± 0.2	0.9 ± 0.2	0.9 ± 0.2	0.3 ± 0.1			

TABLE A-3. Computations of photon absorption and escape for a cylindrical cloud.

Point Source Location (x,y,z)	Percent Escape Through Cloud Face						Total Absorption in % α	Optical Parameters		
	1	2	3	4	5	6		ω_0	g	τ
.50,.50,.50	17.8 ± 1.0	17.8 ± 1.0	17.8 ± 1.0	17.8 ± 1.0	12.5 ± 0.8	12.5 ± 0.8	4.1 ± 0.5	0.99996	0.84	200
.65,.50,.50	8.4 ± 0.7	31.2 ± 1.2	15.9 ± 0.9	15.9 ± 0.9	12.8 ± 0.9	12.8 ± 0.9	3.0 ± 0.4			
.75,.50,.50	5.1 ± 0.6	47.5 ± 1.3	11.5 ± 0.8	11.5 ± 0.8	10.5 ± 0.8	10.5 ± 0.8	3.3 ± 0.5			
.85,.50,.50	2.9 ± 0.4	66.5 ± 1.2	7.8 ± 0.7	7.8 ± 0.7	6.5 ± 0.6	6.5 ± 0.6	2.1 ± 0.4			
.99,.50,.50	0.5 ± 0.2	93.0 ± 0.7	1.4 ± 0.3	1.4 ± 0.3	1.4 ± 0.3	1.4 ± 0.3	0.7 ± 0.2			
.65,.50,.65	8.1 ± 0.7	29.7 ± 1.2	13.8 ± 0.9	13.8 ± 0.9	6.3 ± 0.6	25.5 ± 0.6	2.9 ± 0.4	0.99996	0.84	200
.75,.50,.75	4.1 ± 0.5	42.3 ± 1.3	10.2 ± 0.8	10.2 ± 0.8	2.3 ± 0.4	27.8 ± 1.1	3.1 ± 0.4			
.85,.50,.85	1.4 ± 0.3	48.4 ± 1.3	4.7 ± 0.5	4.7 ± 0.5	0.7 ± 0.2	39.1 ± 1.3	1.0 ± 0.3			
.99,.50,.99	———	49.8 ± 1.3	0.2 ± 0.1	0.2 ± 0.1	———	49.8 ± 1.3	0.1 ± 0.1			
.50,.50,.65	16.0 ± 0.9	16.0 ± 0.9	16.0 ± 0.9	16.0 ± 0.9	6.7 ± 0.6	26.7 ± 1.1	2.5 ± 0.4	0.99996	0.84	200
.50,.50,.75	13.4 ± 0.9	13.4 ± 0.9	13.4 ± 0.9	13.4 ± 0.9	4.4 ± 0.3	38.8 ± 1.2	3.2 ± 0.5			
.50,.50,.85	9.1 ± 0.8	9.1 ± 0.8	9.1 ± 0.8	9.1 ± 0.8	2.0 ± 0.4	59.3 ± 1.2	2.2 ± 0.4			
.50,.50,.99	1.9 ± 0.4	1.9 ± 0.4	1.9 ± 0.4	1.9 ± 0.4	0.3 ± 0.1	91.1 ± 0.7	1.0 ± 0.3			

REFERENCES

Aida, M., 1977: Scattering of solar radiation as a function of cloud dimensions and orientation. *J. Quant. Spectrosc. Radiat. Transfer*, **17**, 303-310.

Brook, M., and N. Kitagawa, 1960: Electric field changes and the design of lightning-flash counters. *J. Geophys. Res.*, **65**, 1927-1931.

———, and T. Ogawa, 1977: The cloud discharge, in *Lightning, Vol. 1, Physics of Lightning*, Academic Press.

———, R. Tennis, C. Rhodes, P. Krehbiel, B. Vonnegut, and O. H. Vaughan, Jr., 1980: Simultaneous observations of lightning radiations from above and below clouds. *Geophys. Res. Lett.*, **7**, 267-270.

Bucher, E. A., 1973: Computer simulation of light pulse propagation for communication through thick clouds. *Appl. Optics*, **12**, 2391-2400.

Byers, H. R., and R. R. Braham, 1949: *The Thunderstorm - Report of the Thunderstorm Project*. Government Printing Office, Washington, D.C.

Chandrasekhar, S., 1950: *Radiative Transfer*. Oxford University Press, 393 pp.

Clegg, R. J., 1971: A photoelectric detector of lightning. *J. Atmos. & Terr. Phys.*, **33**, 1431-1439.

Danielson, R. E., D. R. Moore, and H. C. van de Hulst, 1976: The transfer of visible radiation through clouds. *J. Atmos. Sci.*, **26**, 1078-1087.

Davies, R., 1978: The effect of finite geometry on the three-dimensional transfer of solar irradiance in clouds. *J. Atmos. Sci.*, **35**, 1712-1725.

Davis, J. M., S. K. Cox, and T. B. McKee, 1979: Vertical and horizontal distributions of solar absorption in finite clouds. *J. Atmos. Sci.*, **36**, 1976-1984.

Edgar, B. C., 1978: Global lightning distribution at dawn and dusk for August-December, 1977, as observed by the DMSP lightning detector. The Aerospace Corp., Space Sciences Laboratory, Rept. SSL-78 (3639-02)-1, August.

———, 1980 (in press): The distribution of lightning superbolts. *Proc. VIth Int. Conf. Atmos. Elect.*, Manchester.

Griffiths, R. F., and B. Vonnegut, 1975: Tape recorder photocell instrument for detecting and recording lightning strokes. *Weather*, **30**, 254-257.

Hale, G. M., and M. R. Querry, 1973: Optical constants of water in the 200 nm to 200 μm wavelength region. *Applied Optics*, **12**, 555.

Hansen, J. E., 1971: Multiple scattering of polarized light in planetary atmospheres. Part II: Sunlight reflected by terrestrial water clouds. *J. Atmos. Sci.*, **28**, 1400-1426.

———, and L. D. Travis, 1974: Light scattering in planetary atmospheres. *Space Sci. Rev.*, **16**, 527-610.

Irvine, W. M., and D. B. Pollack, 1968: Infrared optical properties of water and ice spheres. *Icarus*, **8**, 324-360.

Jacobson, E. A., and E. P. Krider, 1976: Electrostatic field changes produced by Florida lightning. *J. Atmos. Sci.*, **33**, 103-117.

Kidder, R. E., 1973: The location of lightning flashes at ranges less than 100 km. *J. Atmos. Terr. Phys.*, **35**, 283-290.

Kitagawa, N., and M. Brook, 1960: A comparison of intracloud and cloud-to-ground lightning discharges. *J. Geophys. Res.*, **65**, 1189-1201.

———, and M. Kobayashi, 1959: Field changes and variations in luminosity due to lightning flashes, in *Recent Advances in Atmospheric Electricity*, Pergamon, 485-501.

Krehbiel, P. R., M. Brook, and R. A. McCrory, 1979: An analysis of the charge structure of lightning discharges to ground. *J. Geophys. Res.*, **84**, 2432-2456.

Krider, E. P., 1966: Some photoelectric observations of lightning. *J. Geophys. Res.*, **71**, 3095-3098.

———, 1974: The relative light intensity produced by a lightning stepped-leader. *J. Geophys. Res.*, **79**, 4542-4544.

Mackerras, D., 1973: Photoelectric observations of the light emitted by lightning flashes. *J. Atmos. & Terr. Phys.*, **35**, 521-535.

Magono, C., 1980: *Thunderstorms*. Elsevier Scientific Publishing Co.

McKee, T. B., and S. K. Cox, 1974: Scattering of visible radiation by finite clouds. *J. Atmos. Sci.*, **31**, 1885-1892.

Orville, R. E., 1981: Global distribution of midnight lightning - September to November, 1977. *Mon. Wea. Rev.*, **109**, 391-395.

———, and D. W. Spencer, 1979: Global lightning flash frequency. *Mon. Wea. Rev.*, **107**, 934-943.

Plass, G. N., and G. W. Kattawar, 1968: Monte Carlo calculations of light scattering from clouds. *Appl. Optics*, **1**, 126-130.

Proctor, D. E., 1971: A hyperbolic system for obtaining VHF radio pictures of lightning. *J. Geophys. Res.*, **76**, 1478-1489, 1971.

———, 1981: VHF radio pictures of cloud flashes. *J. Geophys. Res.*, **86**, 4041-4071.

Rozenberg, G. V., 1968: Optical investigations of atmospheric aerosol. *Sov. Phys. Uspekhi*, **11**, 353-380.

Salanave, L. E., 1980: *Lightning and Its Spectrum*. University of Arizona Press, Tucson.

Sparrow, J. G., and E. P. Ney, 1968: Discrete light sources observed by satellite OSO-B. *Science*, **161**, 459-460.

Taylor, W. L., 1978: A VHF technique for space-time mapping of lightning discharge processes. *J. Geophys. Res.*, **83**, 3575-3583.

Teer, T. L., and A. A. Few, 1974: Horizontal lightning. *J. Geophys. Res.*, **79**, 3436-3441.

Turman, B. N., 1977: Detection of lightning superbolts. *J. Geophys. Res.*, **82**, 2566-2568.

———, 1978: Analysis of lightning data from the DMSP satellite. *J. Geophys. Res.*, **83**, 5019-5024.

———, 1979: Lightning detection from space. *Amer. Sci.*, **67**, 321-329.

———, and R. J. Tettelbach, 1980: Synoptic-scale satellite lightning observations in conjunction with tornados. *Mon. Wea. Rev.*, **108**, 1878-1882.

———, and B. C. Edgar, 1981: Global lightning distributions at dawn and dusk. To be published *J. Geophys. Res.*

Twomey, S., 1971: Radiative transfer: Terrestrial clouds. *J. Quant. Spectrosc. Radiat. Transfer*, **11**, 779-783.

———, 1977: *Atmospheric Aerosols*. Elsevier.

———, and C. F. Bohren, 1980: Simple approximations for calculations of absorption in clouds. *J. Atmos. Sci.*, **37**, 2086-2094.

———, H. Jacobowitz, and H. B. Howell, 1967: Light scattering by cloud layers. *J. Atmos. Sci.*, **24**, 70-79, 1967.

Uman, M. A., 1969: *Lightning*. McGraw-Hill.

Van Blerkom, D., 1971: Diffuse reflection from clouds with horizontal inhomogeneities. *Astrophys. J.*, **166**, 235-242.

van de Hulst, H. C., 1957: *Light Scattering by Small Particles*. Wiley.

———, 1980: *Multiple Scattering Tables, Formulas and Applications*, Vols. 1 and 2, Academic Press.

———, and K. Grossman, 1968: Multiple light scattering in planetary atmospheres, in *The Atmospheres of Venus and Mars*, ed. by J. C. Brandt and M. B. McElroy. Gordon and Breach.

Vonnegut, B., and R. E. Passarelli, Jr., 1978: Modified time sound camera for photographing thunderstorms and recording lightning. *J. Appl. Meteor.*, **17**, 1079-1081.

Vorphal, J. A., J. G. Sparrow, and E. P. Ney, 1970: Satellite observations of lightning. *Science*, **169**, 860-862.

Wolfe, W. L., and G. J. Zissis, 1978: *The Infrared Handbook*. Environmental Research Institute of Michigan.

FIGURE CAPTIONS

Fig. 1. The solid curve shows the fractional absorption, α, of a semi-infinite cloud layer with vertical incidence (Twomey and Bohren, 1980). The dots and bars are the means and standard deviations computed using our Monte Carlo simulation.

Fig. 2. a) Distribution of reflected photons vs. zenith angle, Z, from conservative cloud layers with normal incidence. The fraction is for a cos(Z) interval of 0.1. The scaled optical depth in all three examples equals 6.

b) Same as a) except the scaled optical depth is 12.

Fig. 3. The mean optical path length, $\bar{\tau}$, of reflected and transmitted photons vs. optical depth from Twomey *et al.* (1967) [solid curves] and the results of Monte Carlo simulations [solid symbols].

Fig. 4. Reflectance of vertically incident photons as determined by the Monte Carlo program of McKee and Cox (1974) [solid and dashed curves] and our Monte Carlo results [solid dots].

Fig. 5. Sketches of (a) the cubical, (b) the spherical, and (c) the cylindrical cloud geometries used in this study. The numbers label the cloud faces, and the solid dots show the point-source locations computed for that geometry.

Fig. 6. (a-h) Top views of the channel geometries derived from point sources in the horizontal plane (z = 0.5).

Fig. 7. Total absorption vs. position for point sources located along the line (x, 0.5, 0.5) in a cubical cloud. Note that the absorption is symmetric about x = 0.5.

Fig. 8. The fraction of photons escaping face 2 of the cube vs. point source position along the (x, 0.5, 0.5) axis.

Fig. 9. The sum of the fractions escaping through faces 3, 4, 5, and 6 of the cube vs. source position along the line (x, 0.5, 0.5).

Fig. 10. Distributions of emerging zenith angles, Z, for photons which escape through faces 5 and 6 of the cube. The fractions are for cos(Z) intervals of 0.1.

Fig. 11. Same as Fig. 10 except for faces 1, 2, 3, and 4.

Fig. 12. Distributions of the azimuth angles of photons which escape through faces 1, 2, 3 and 4. The fractions are for azimuth intervals of 0.1π radians.

Fig. 13. Distributions of the optical paths traveled by photons emitted from various point sources within a cubical cloud of total optical depth 200.

Fig. 14. Same as Fig. 13 except for a total optical depth 400.

Fig. 15. The most probable optical path, τ_{mp}, and the mean optical path $\bar{\tau}$ for photons emitted from point sources along the line (x, 0.5, 0.5) in cubical clouds of the specified optical depth.

Fig. 16. The fraction of photons which escape through a region of size S, on face 2 of a cubical cloud; and the hemispheric fraction of photons which escape through a circular region of minimum diameter, S, on the source hemisphere. All sources are located along the (x, 0.5, 0.5) axis; Cu = cube and Sp = sphere.

Fig. 17. The characteristic dimension, S_0, of the region which contains 70% of the photons emitted from cubical and spherical clouds as a function of point-source position along the line (x, 0.5, 0.5).

Fig. 18. Angular dependence of the total cloud intensity for a cubical cloud in the y = 0.5 plane. The fractions are for a solid angle interval of 0.01π steradians at cos(Z) intervals of 0.1.

Fig. 19. Same as Fig. 18, except for a spherical cloud.

Fig. 20. Same as Fig. 18, except for the extended channel sources sketched in Fig. 6.

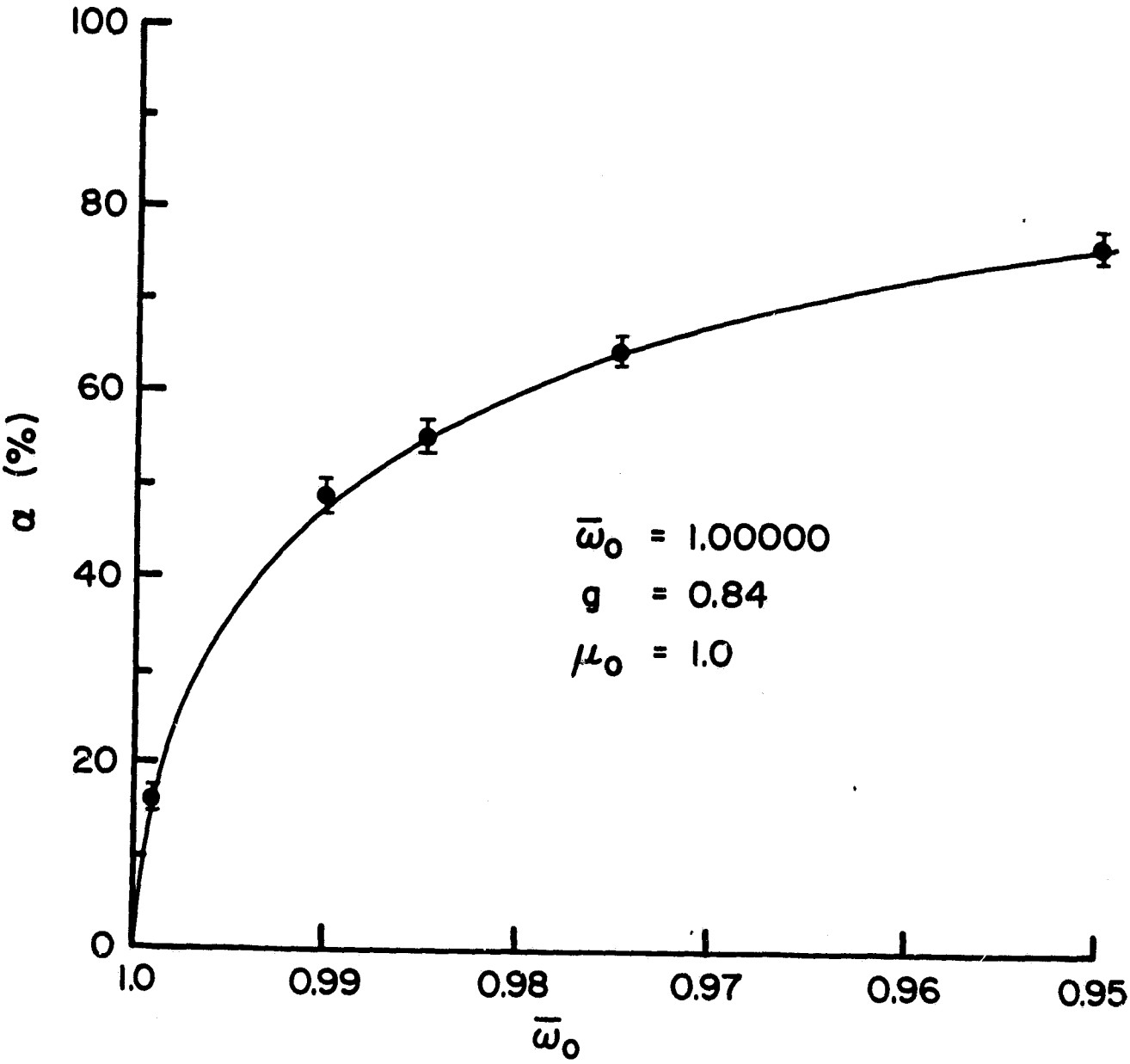
100
80
60
40
20
0
α (%)
$\bar{\omega}_0$ = 1.00000
g = 0.84
μ_0 = 1.0
1.0
0.99
0.98
0.97
0.96
0.95
$\bar{\omega}_0$

Fig. 1

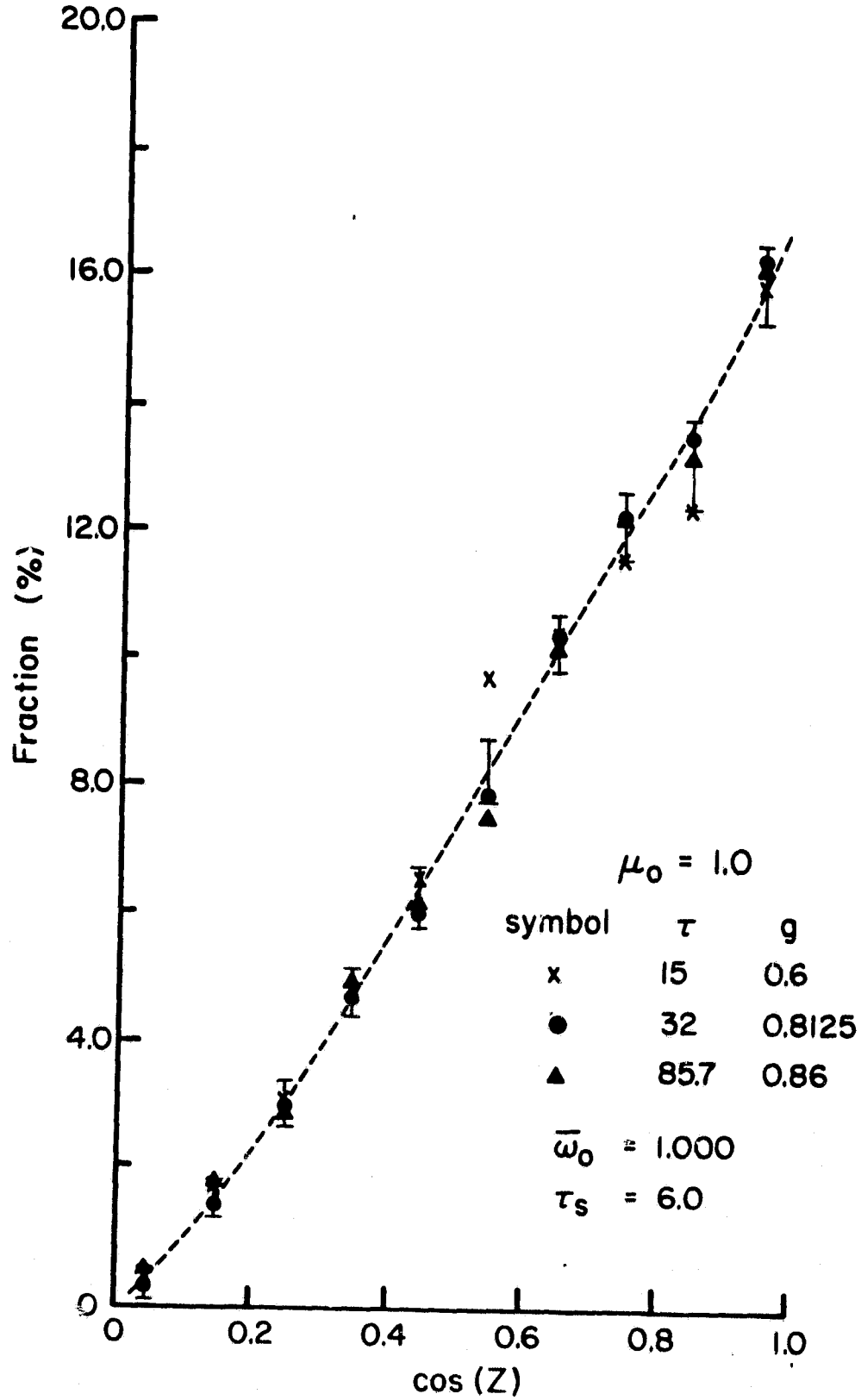
20.0
16.0
12.0
8.0
4.0
0
Fraction (%)
0
0.2
0.4
0.6
0.8
1.0
cos (Z)
μ_0 = 1.0
symbol τ g
x 15 0.6
● 32 0.8125
▲ 85.7 0.86
$\bar{\omega}_0$ = 1.000
τ_s = 6.0

Fig. 2a

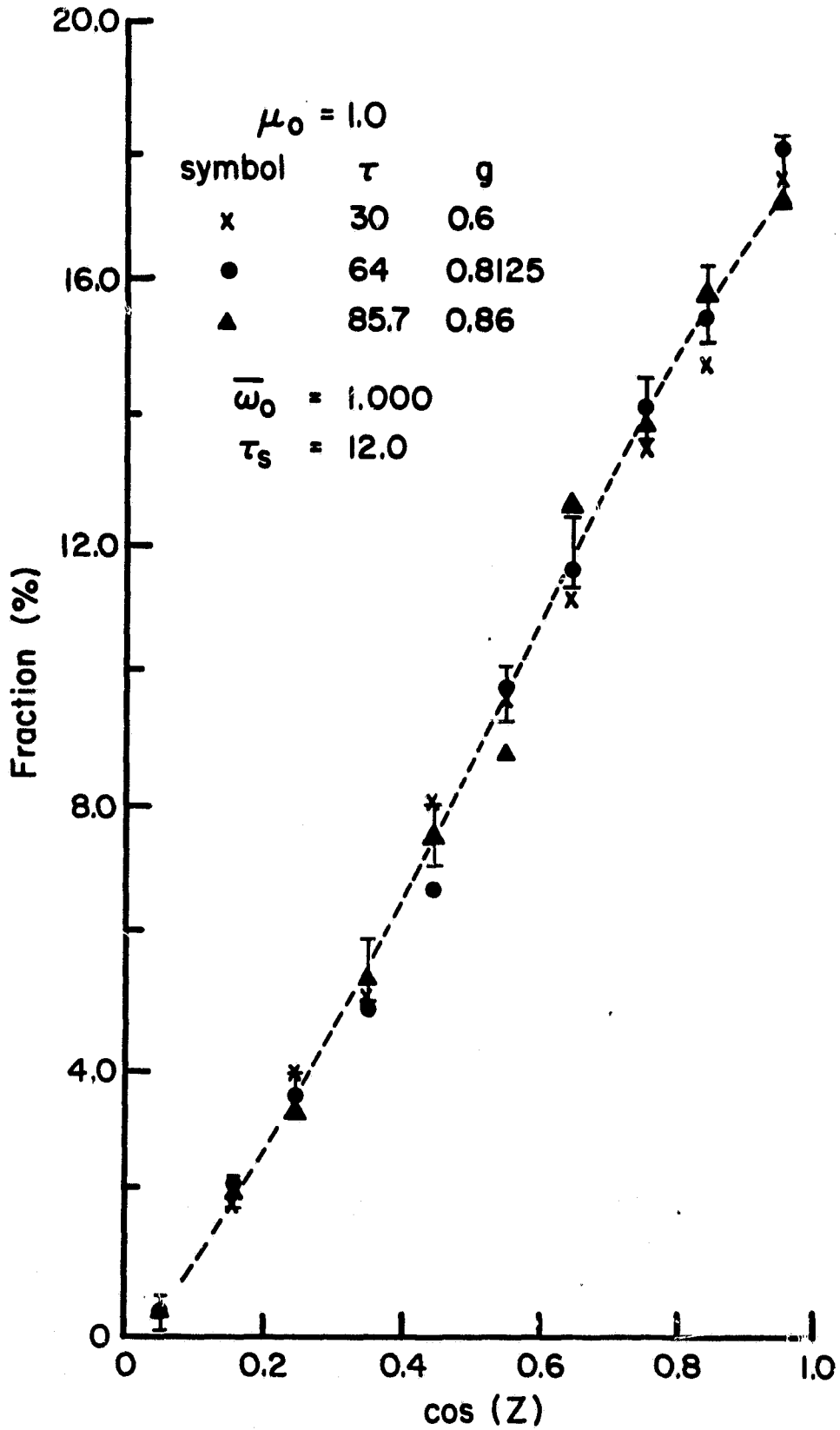
20.0
16.0
12.0
8.0
4.0
0
Fraction (%)
μ_0 = 1.0
symbol τ g
x 30 0.6
● 64 0.8125
▲ 85.7 0.86
$\overline{\omega_0}$ = 1.000
τ_s = 12.0
0
0.2
0.4
0.6
0.8
1.0
cos (Z)

Fig. 2b

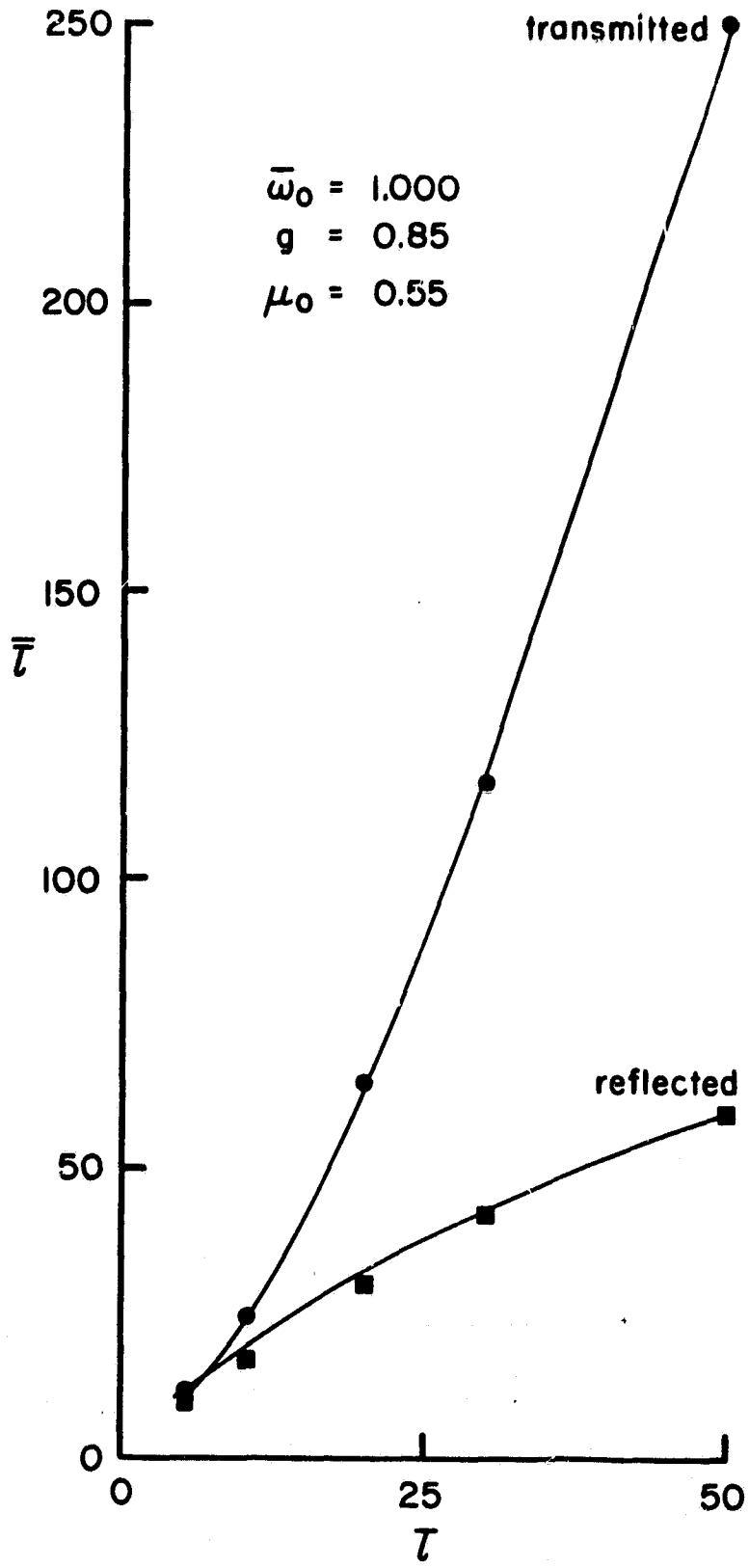
250
200
150
100
50
0
0
25
50
$\bar{\tau}$
τ
$\bar{\omega}_0$ = 1.000
g = 0.85
μ_0 = 0.55
transmitted
reflected

Fig. 3

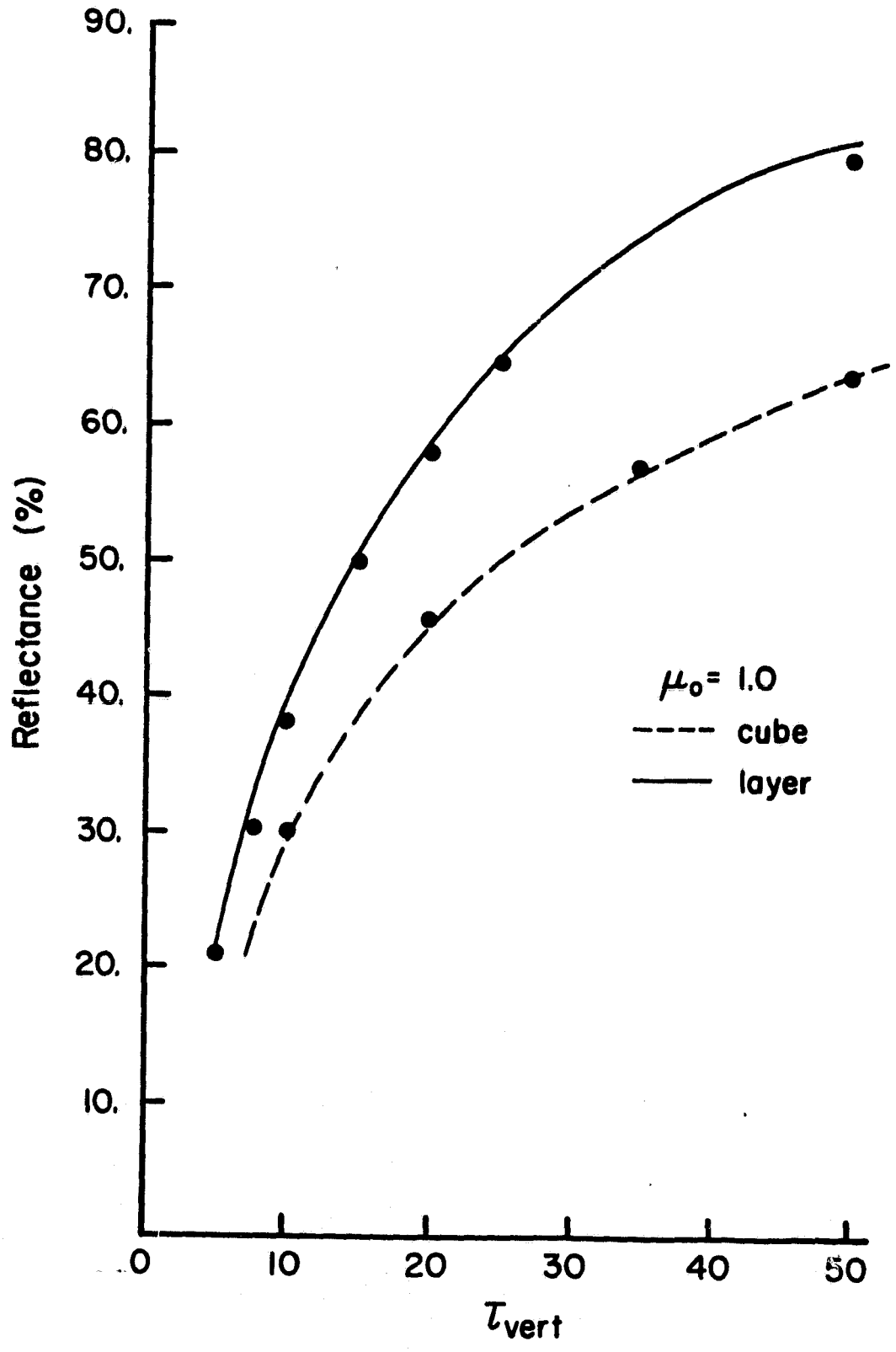
90.
80.
70.
60.
50.
40.
30.
20.
10.
Reflectance (%)
0
10
20
30
40
50
τ_{vert}
μ_0= 1.0
cube
layer

Fig. 4

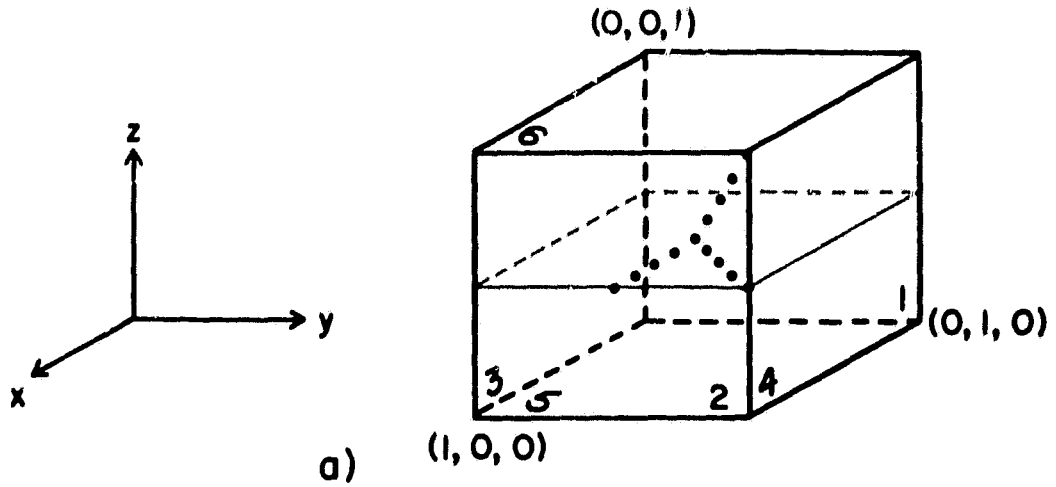
z
y
x
(0, 0, 1)
6
1
(0, 1, 0)
3
5
2
4
(1, 0, 0)

a)

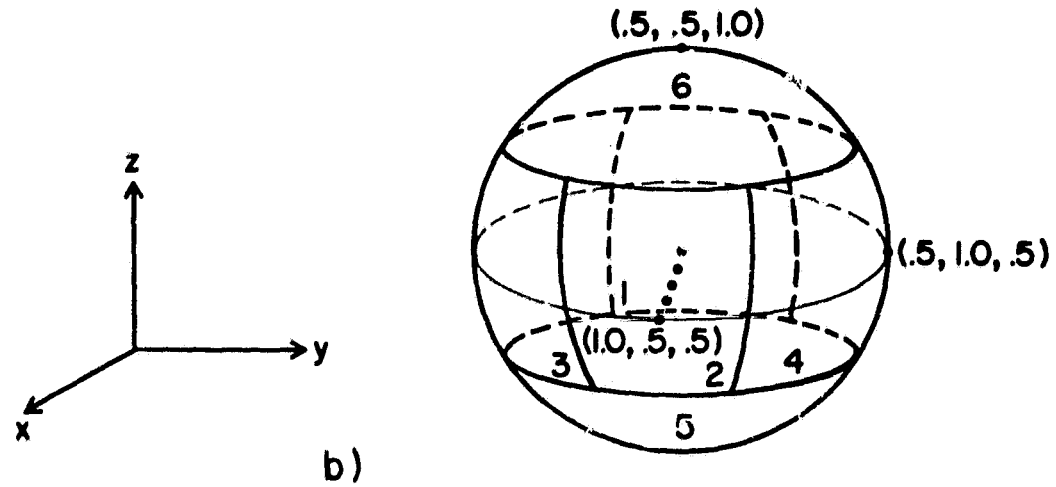
z
y
x
(.5, .5, 1.0)
6
(.5, 1.0, .5)
1
(1.0, .5, .5)
3
2
4
5

b)

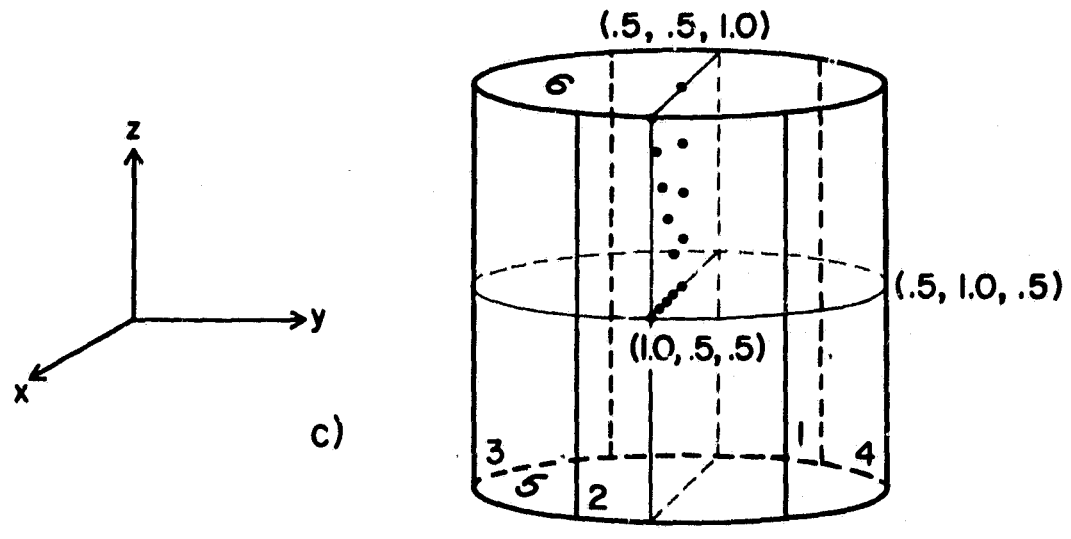
z
y
x
(.5, .5, 1.0)
6
(.5, 1.0, .5)
(1.0, .5, .5)
3
5
2
1
4

c)

Fig. 5

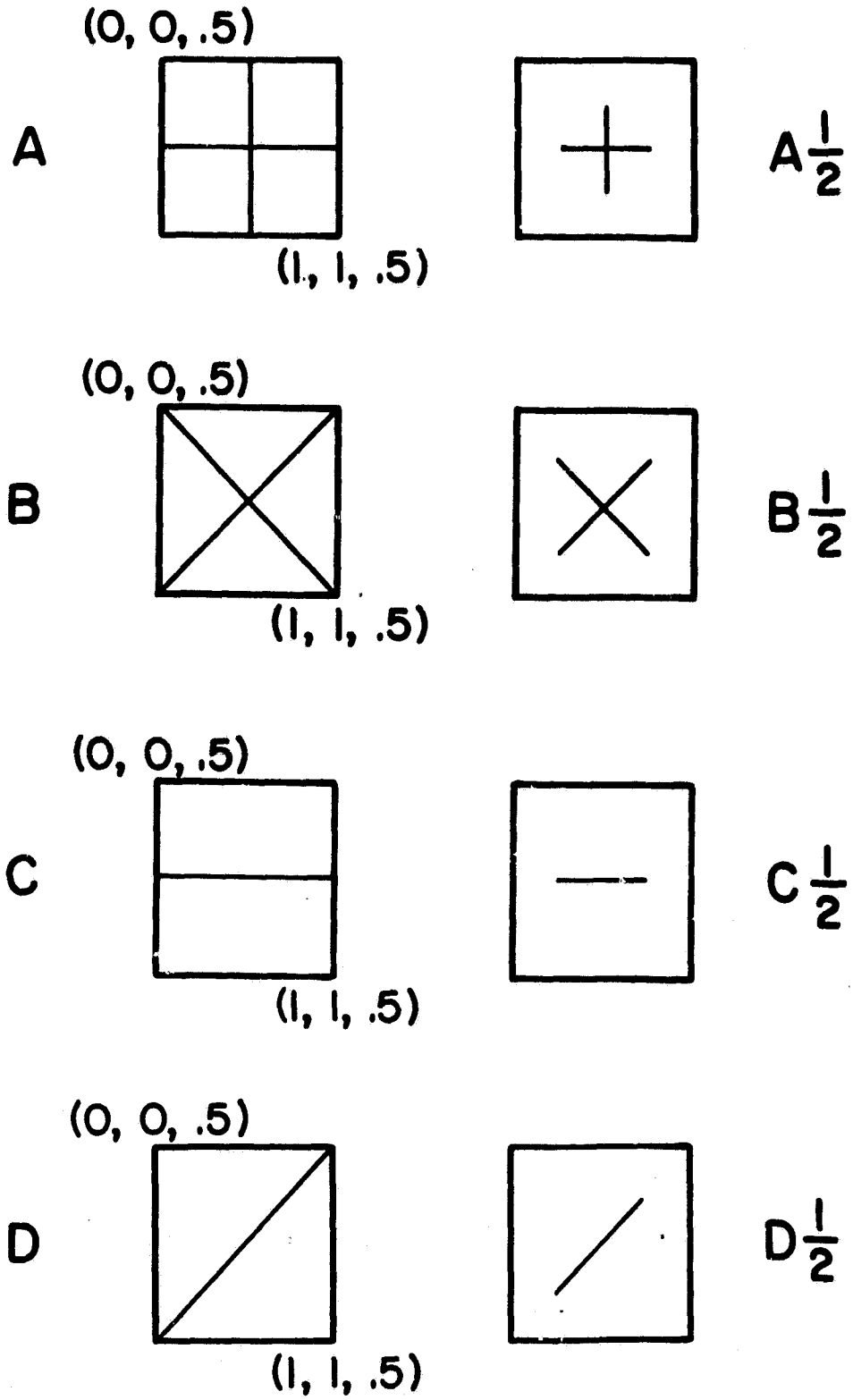

Fig. 6

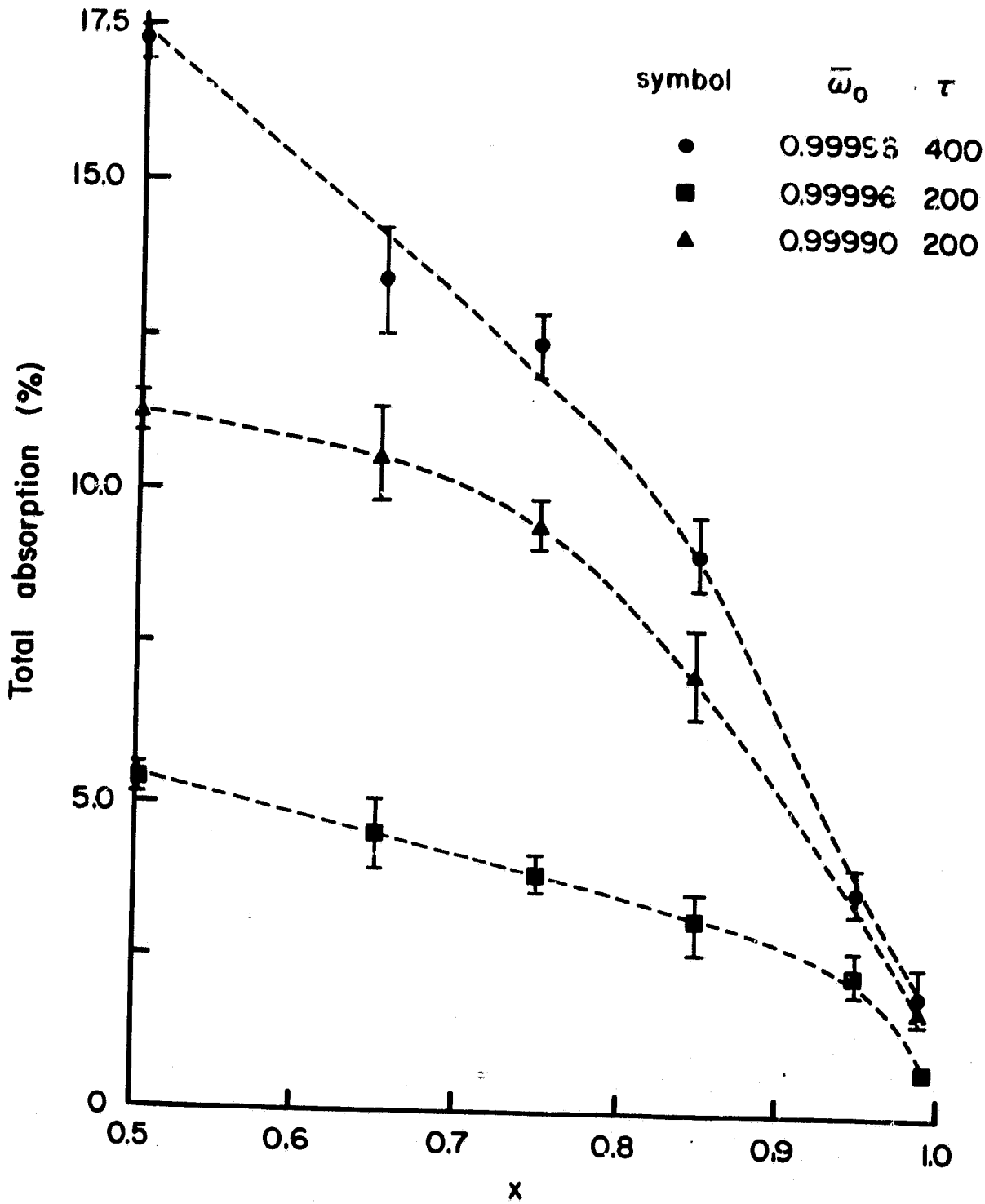
symbol
$\bar{\omega}_0$
τ
0.99996 200
0.99990 200
Total absorption (%)
17.5
15.0
10.0
5.0
0
0.5
0.6
0.7
0.8
0.9
1.0
x

Fig. 7

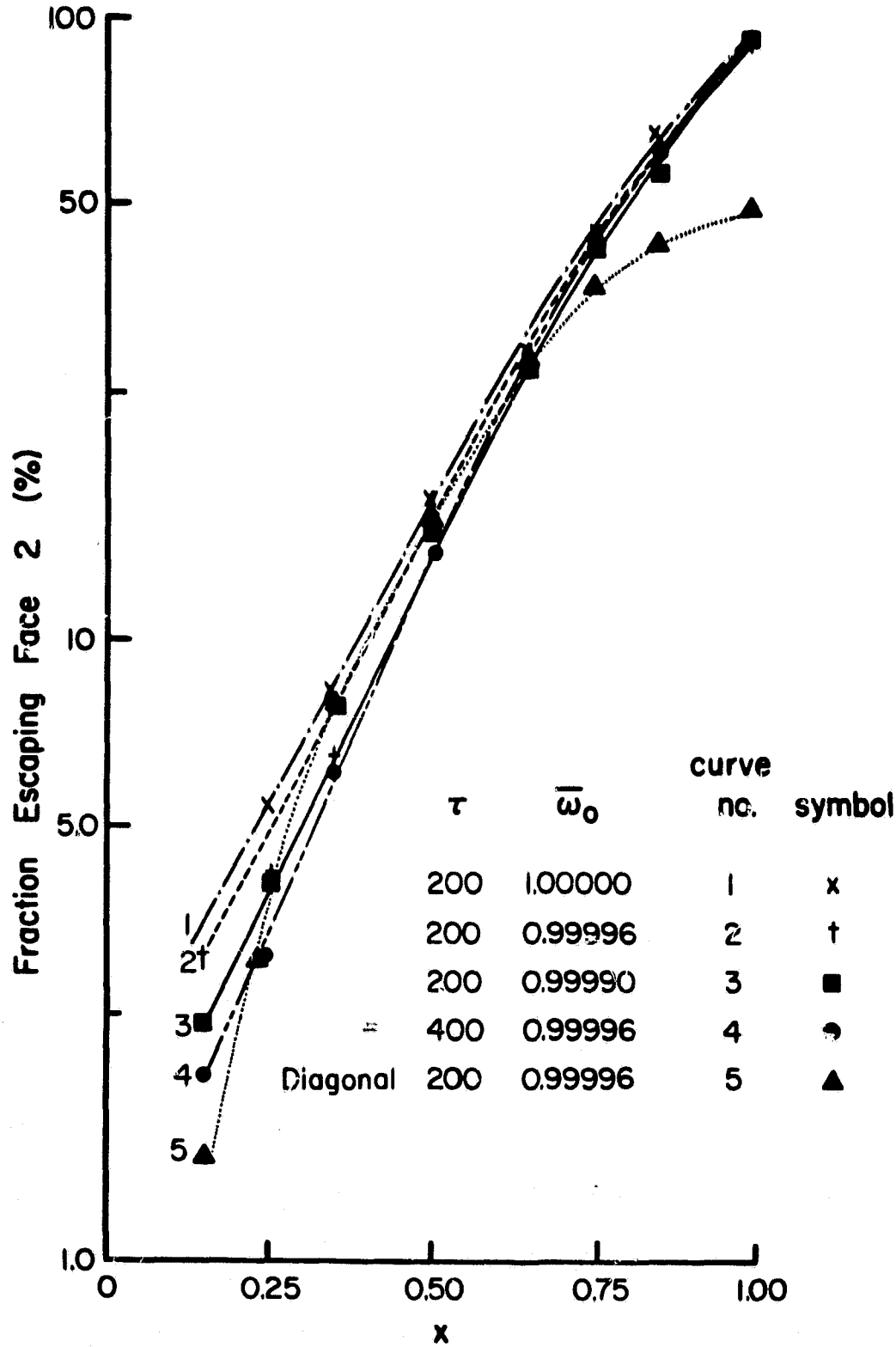
100
50
10
5.0
1.0
Fraction Escaping Face 2 (%)
0
0.25
0.50
0.75
1.00
x
1
2†
3
4
5
τ
$\bar{\omega}_0$
curve no.
symbol
200 1.00000 1 x
200 0.99996 2 †
200 0.99990 3 ■
400 0.99996 4 ●
Diagonal 200 0.99996 5 ▲

Fig. 8

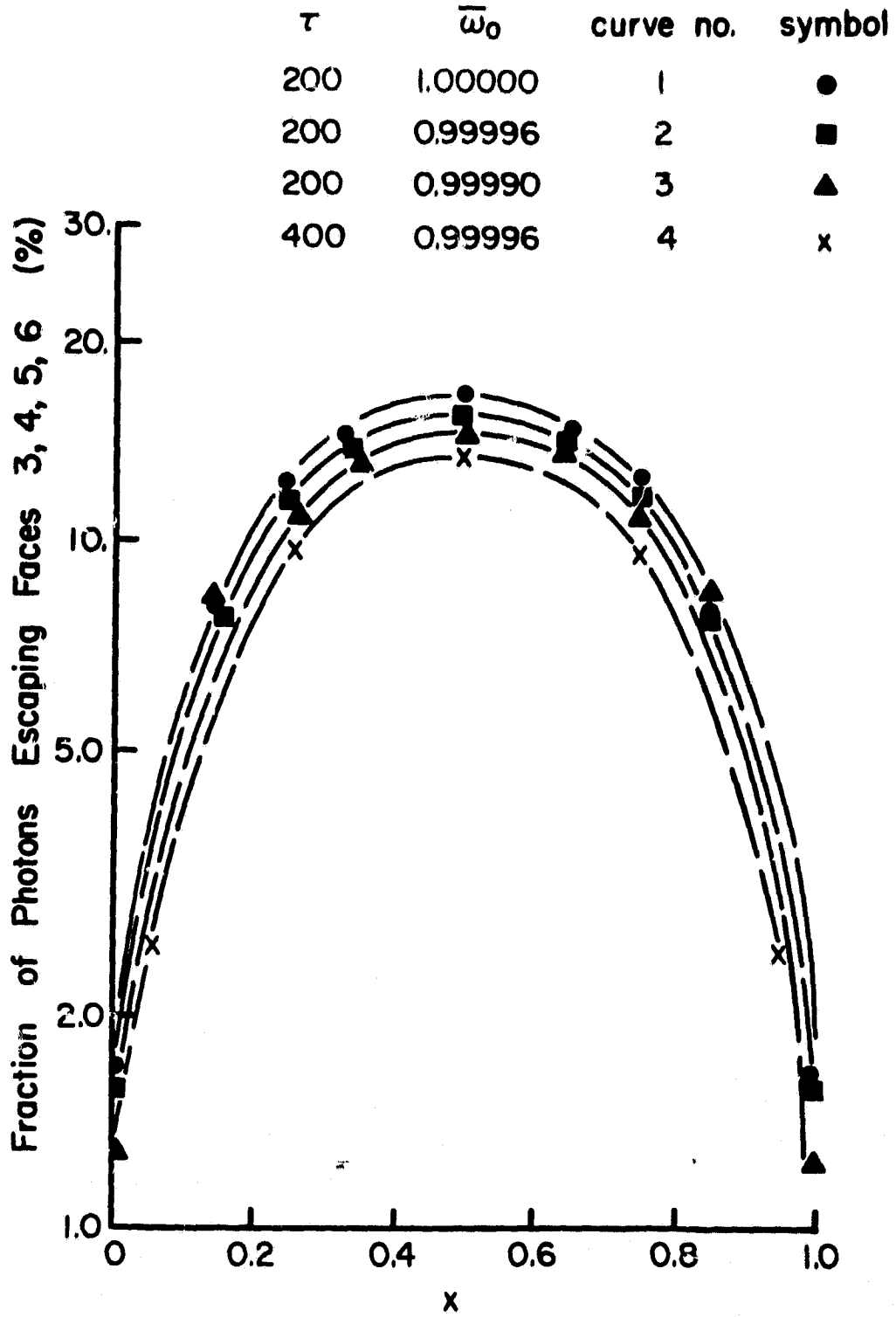
τ
$\bar{\omega}_0$
curve no.
symbol
200
1.00000
1
200
0.99996
2
200
0.99990
3
400
0.99996
4
Fraction of Photons Escaping Faces 3, 4, 5, 6 (%)
30.
20.
10.
5.0
2.0
1.0
0
0.2
0.4
0.6
0.8
1.0
X

Fig. 9

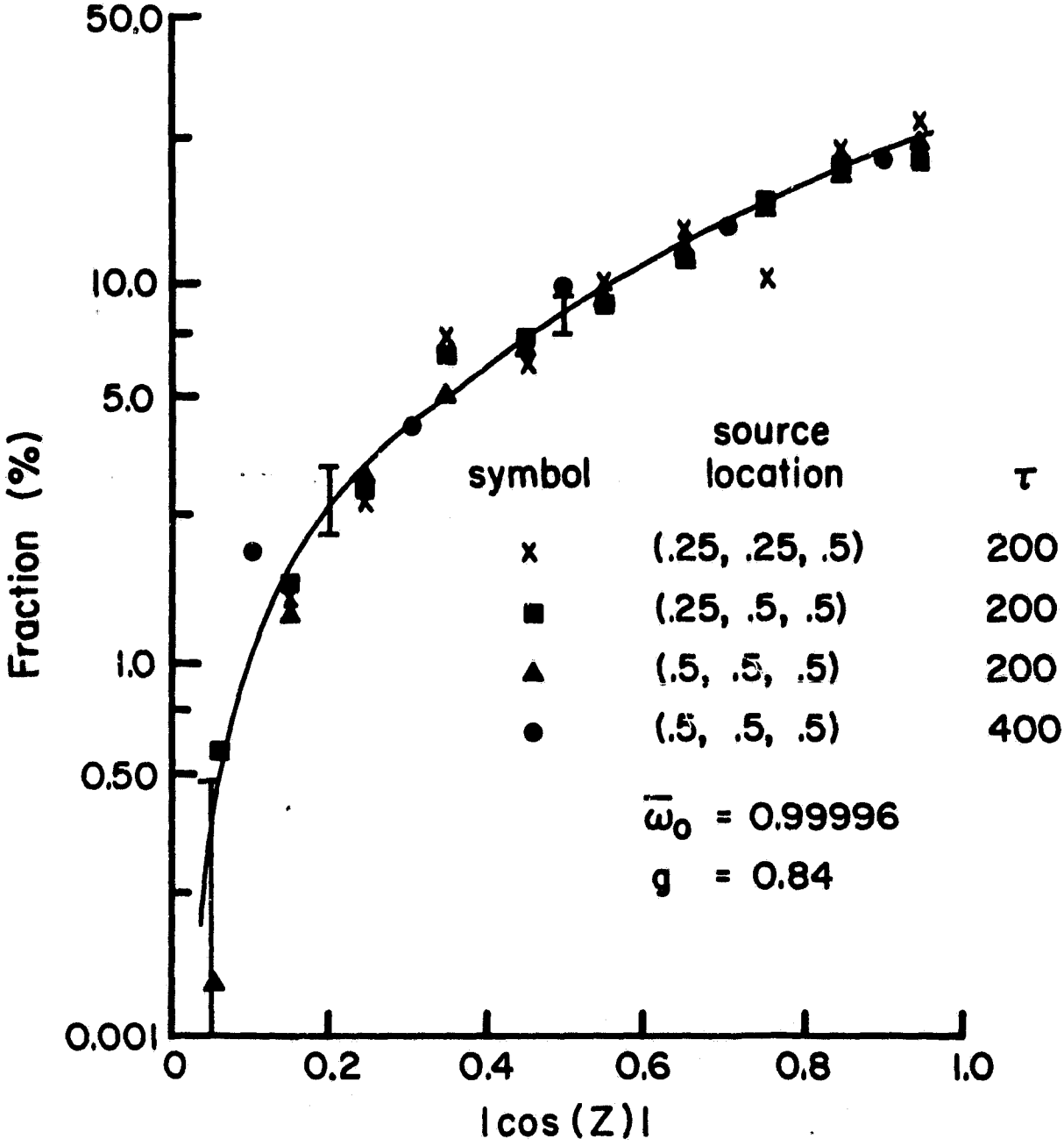
50.0
10.0
5.0
1.0
0.50
0.001
Fraction (%)
0
0.2
0.4
0.6
0.8
1.0
|cos (Z)|
symbol
source location
τ
x (.25, .25, .5) 200
■ (.25, .5, .5) 200
▲ (.5, .5, .5) 200
● (.5, .5, .5) 400
$\bar{\omega}_0$ = 0.99996
g = 0.84

Fig. 10

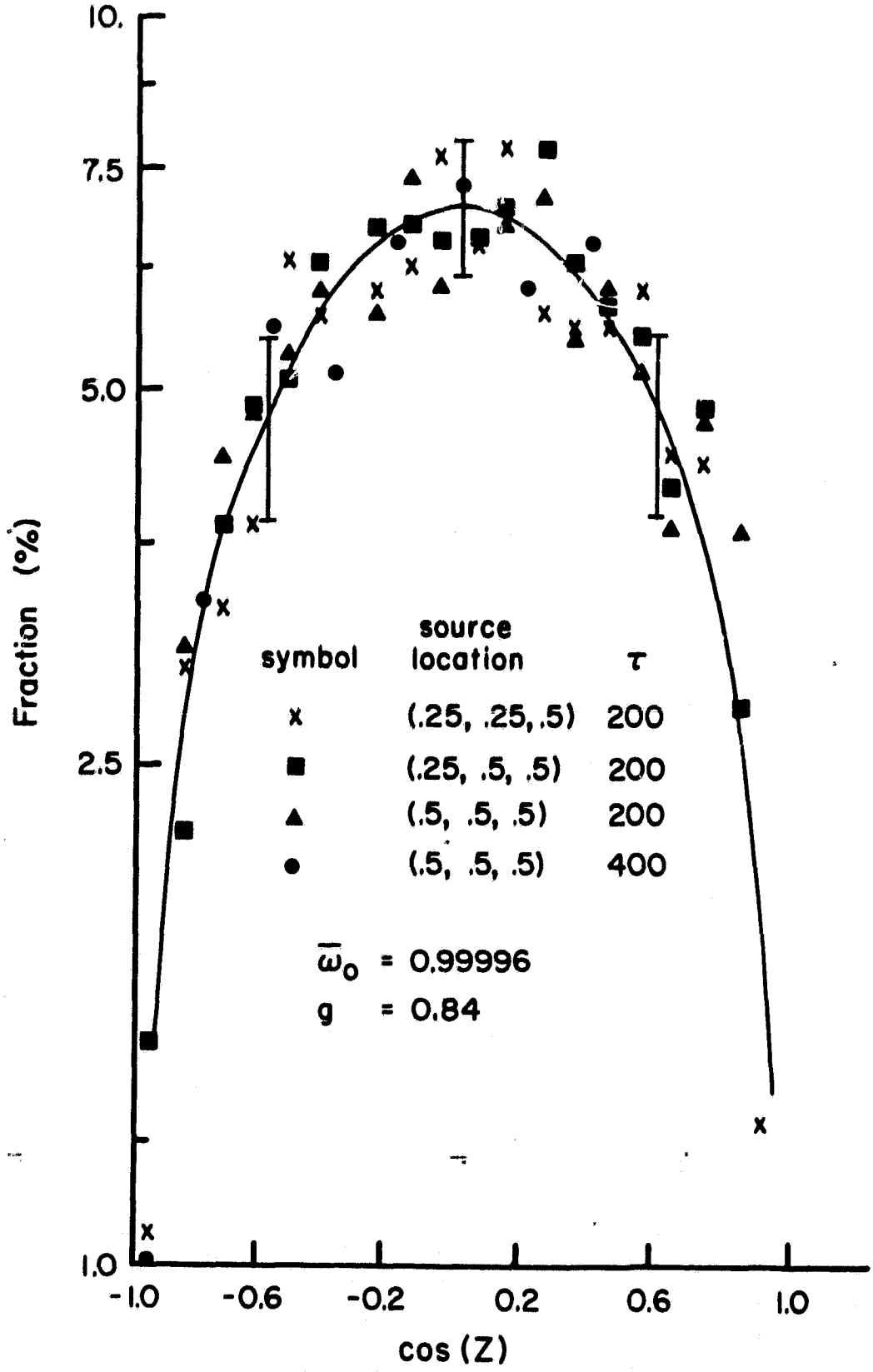
10.
7.5
5.0
2.5
1.0
Fraction (%)
symbol
source location
τ
x (.25, .25, .5) 200
■ (.25, .5, .5) 200
▲ (.5, .5, .5) 200
● (.5, .5, .5) 400
$\bar{\omega}_0$ = 0.99996
g = 0.84
-1.0
-0.6
-0.2
0.2
0.6
1.0
cos (Z)

Fig. 11

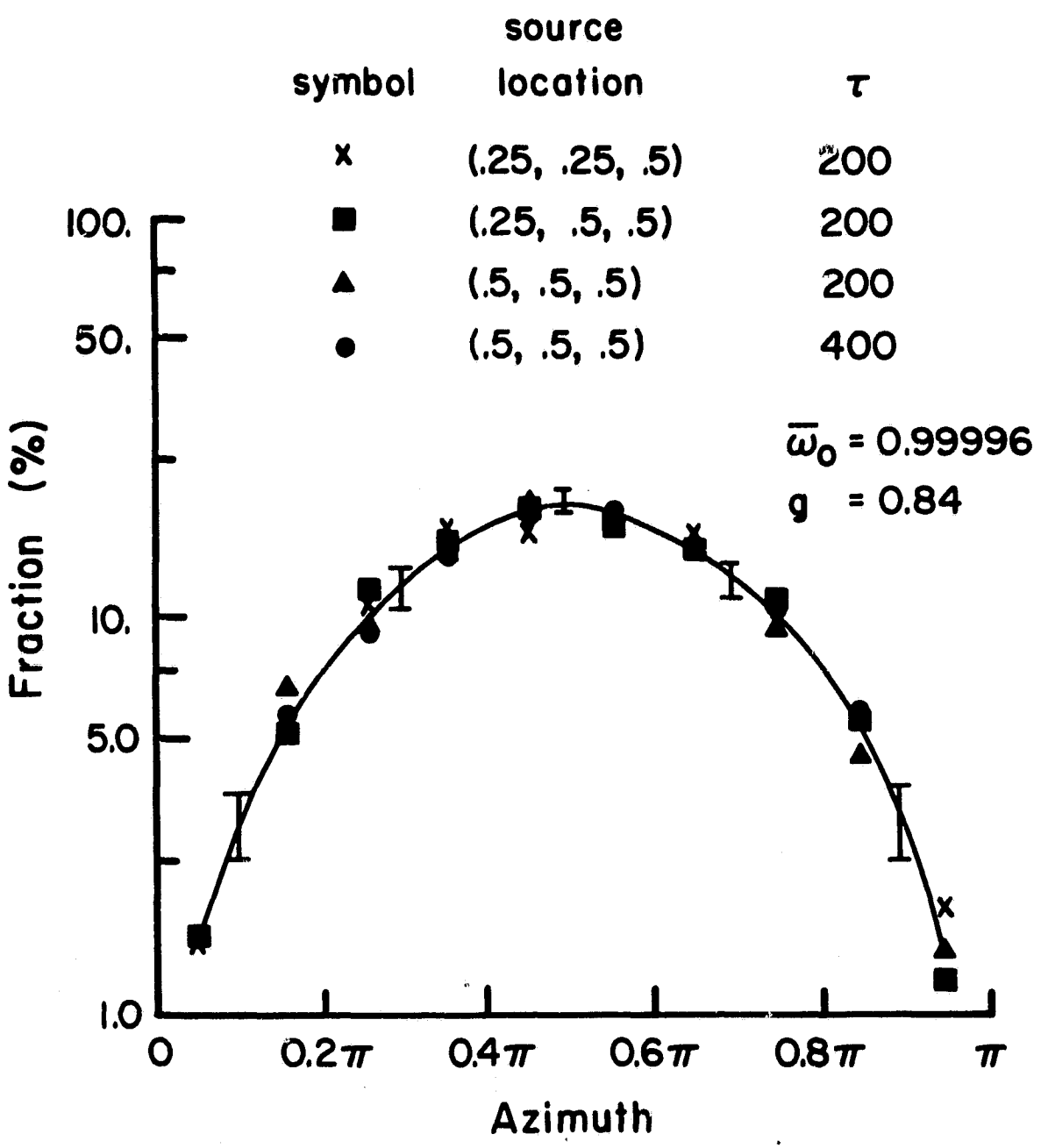
source
symbol
location
τ
(.25, .25, .5) 200
(.25, .5, .5) 200
(.5, .5, .5) 200
(.5, .5, .5) 400
$\bar{\omega}_0$ = 0.99996
g = 0.84
100.
50.
10.
5.0
1.0
Fraction (%)
0
0.2π
0.4π
0.6π
0.8π
π
Azimuth

Fig. 12

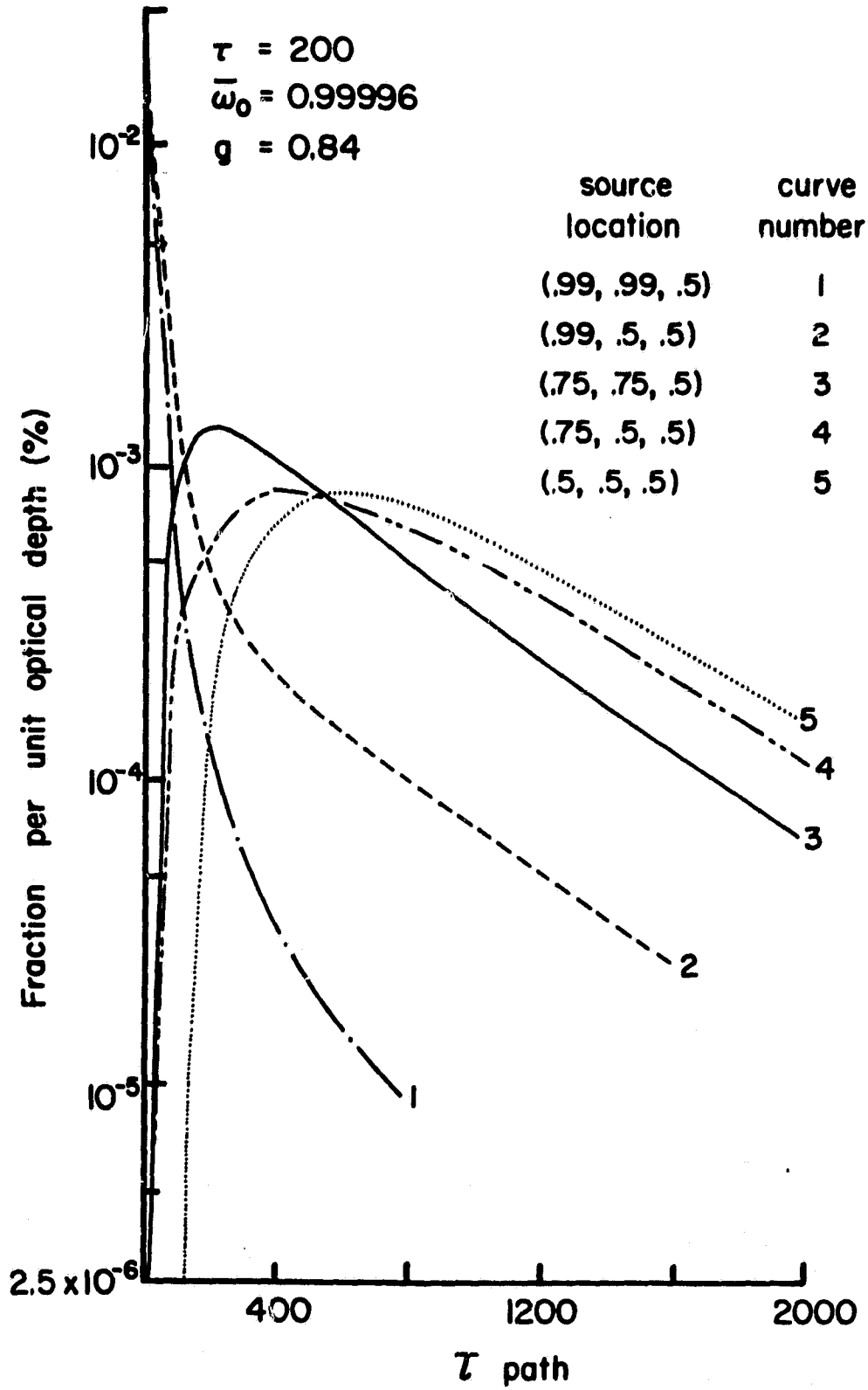
τ = 200
ω̄₀ = 0.99996
g = 0.84
source location
curve number
(.99, .99, .5) 1
(.99, .5, .5) 2
(.75, .75, .5) 3
(.75, .5, .5) 4
(.5, .5, .5) 5
Fraction per unit optical depth (%)
10⁻²
10⁻³
10⁻⁴
10⁻⁵
2.5 x 10⁻⁶
400
1200
2000
τ path

Fig. 13

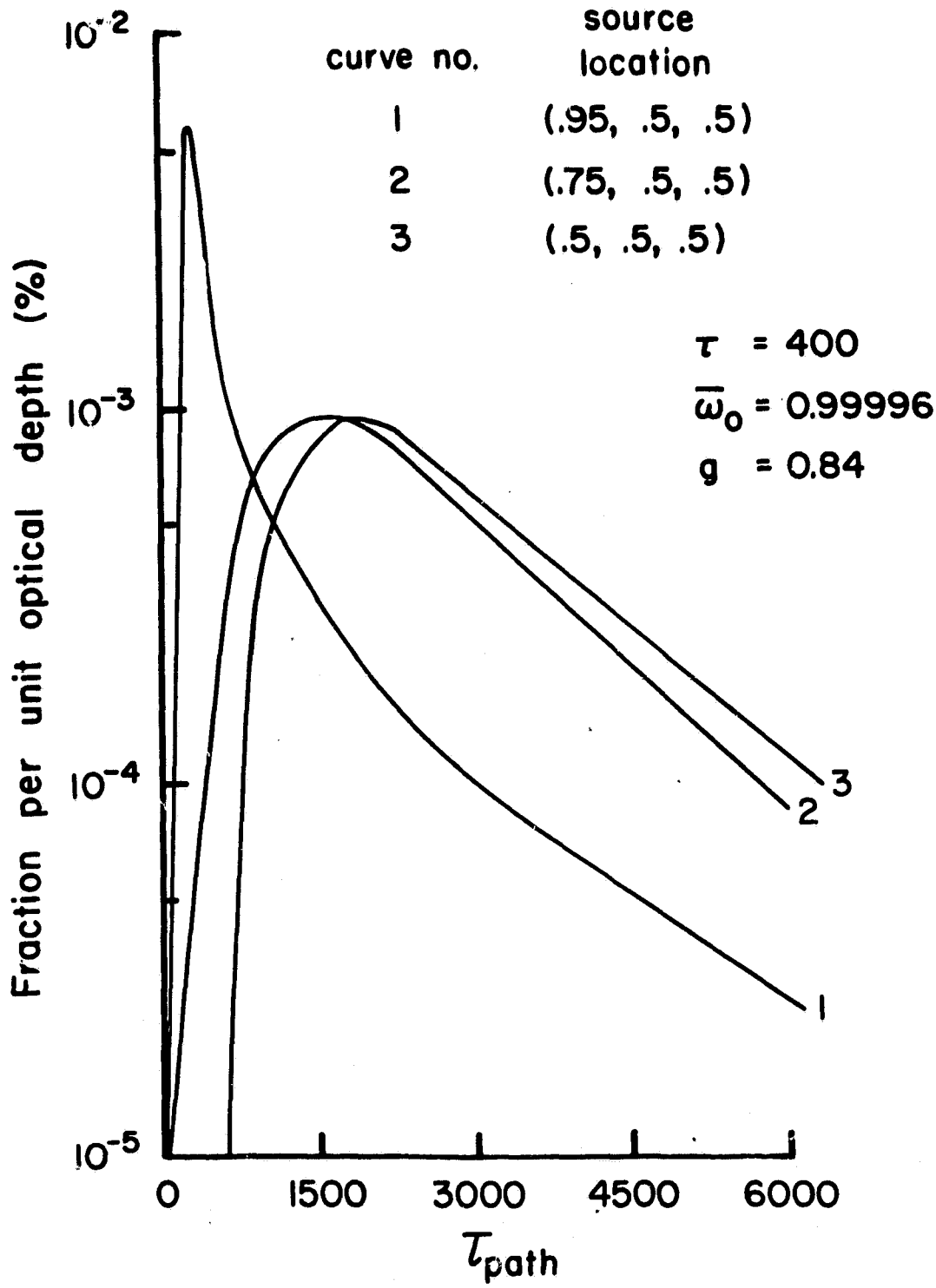
curve no.
source location
1 (.95, .5, .5)
2 (.75, .5, .5)
3 (.5, .5, .5)
τ = 400
ω̄₀ = 0.99996
g = 0.84
Fraction per unit optical depth (%)
10⁻²
10⁻³
10⁻⁴
10⁻⁵
0
1500
3000
4500
6000
τpath
1
2
3

Fig. 14

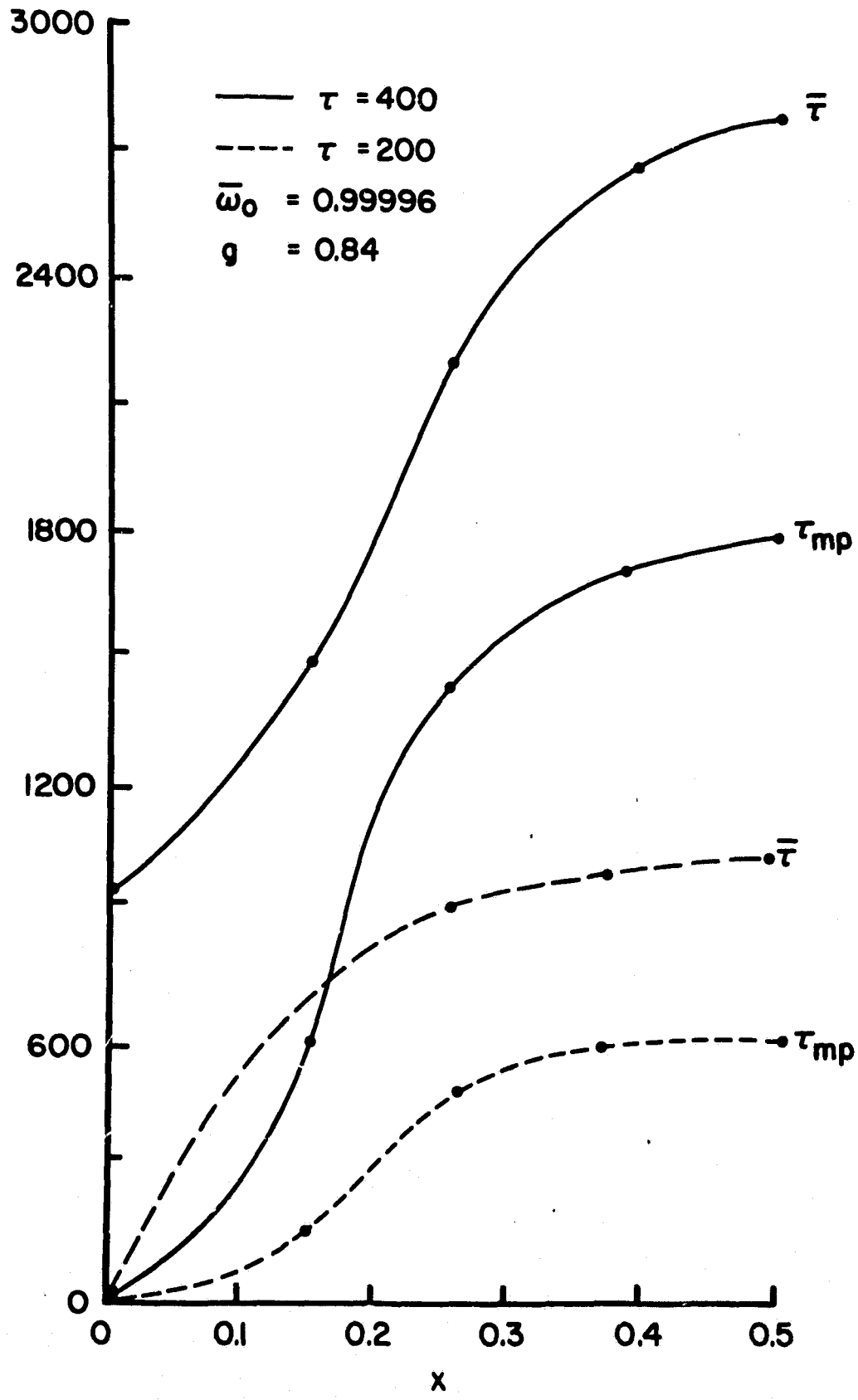
3000
2400
1800
1200
600
0
τ =400
τ =200
ω̄₀ = 0.99996
g = 0.84
τ̄
τmp
τ̄
τmp
0
0.1
0.2
0.3
0.4
0.5
X

Fig. 15

curve no.	geometry	source location (x)	τ
1	Cu	0.01	400
2	Cu	0.01	200
3	Sp	0.01	200
4	Cu	0.05	400
5	Cu	0.25	200
6	Cu	0.50	200
7	Cu	0.50	400
8	Sp	0.25	200
9	Sp	0.50	200

$\bar{\omega}_o = 0.99996$

$g = 0.84$

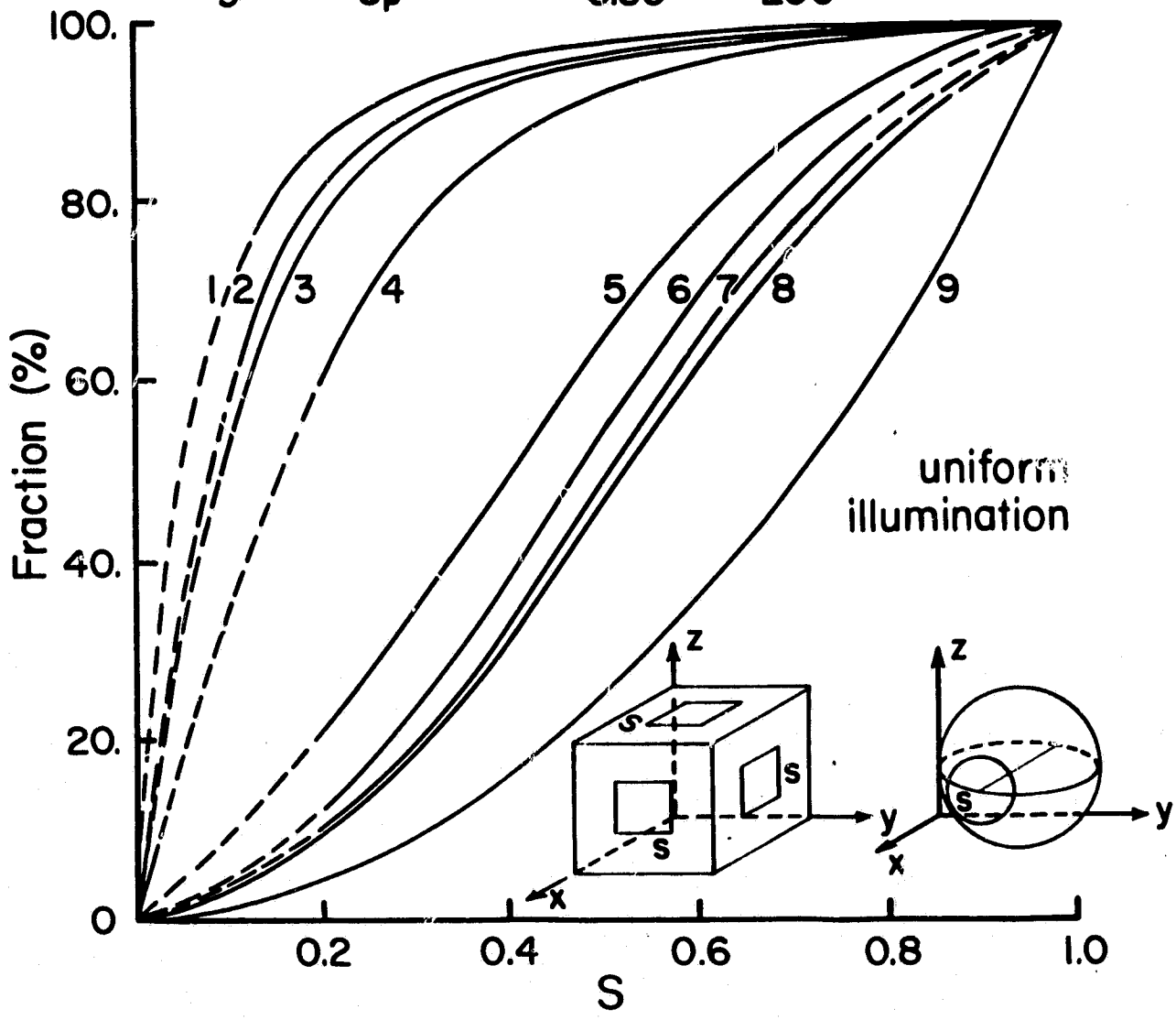

Fig. 16

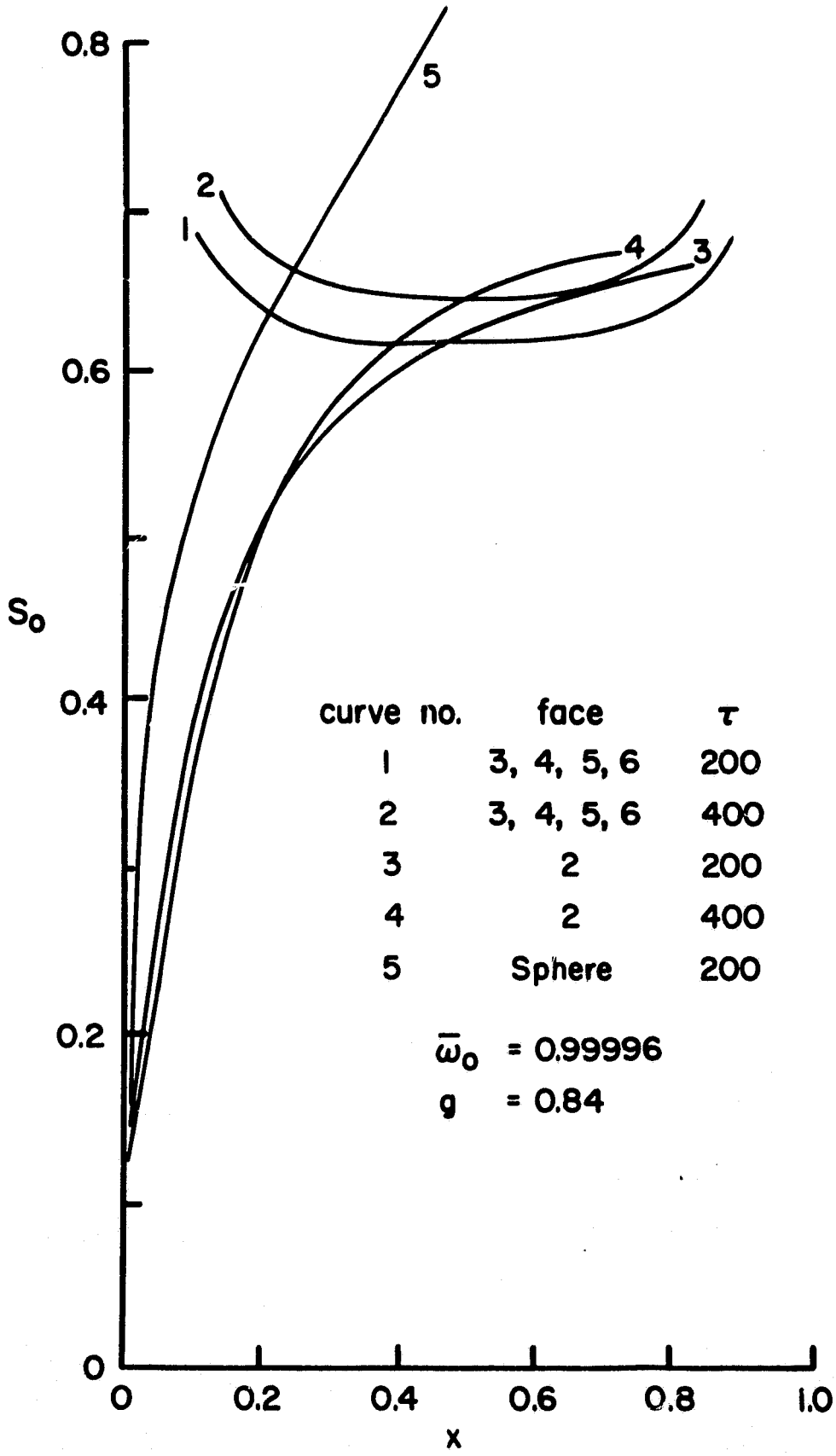
0.8
0.6
0.4
0.2
0
S_o
0
0.2
0.4
0.6
0.8
1.0
x
1
2
3
4
5
curve no. face τ
1 3, 4, 5, 6 200
2 3, 4, 5, 6 400
3 2 200
4 2 400
5 Sphere 200
$\bar{\omega}_o$ = 0.99996
g = 0.84

Fig. 17

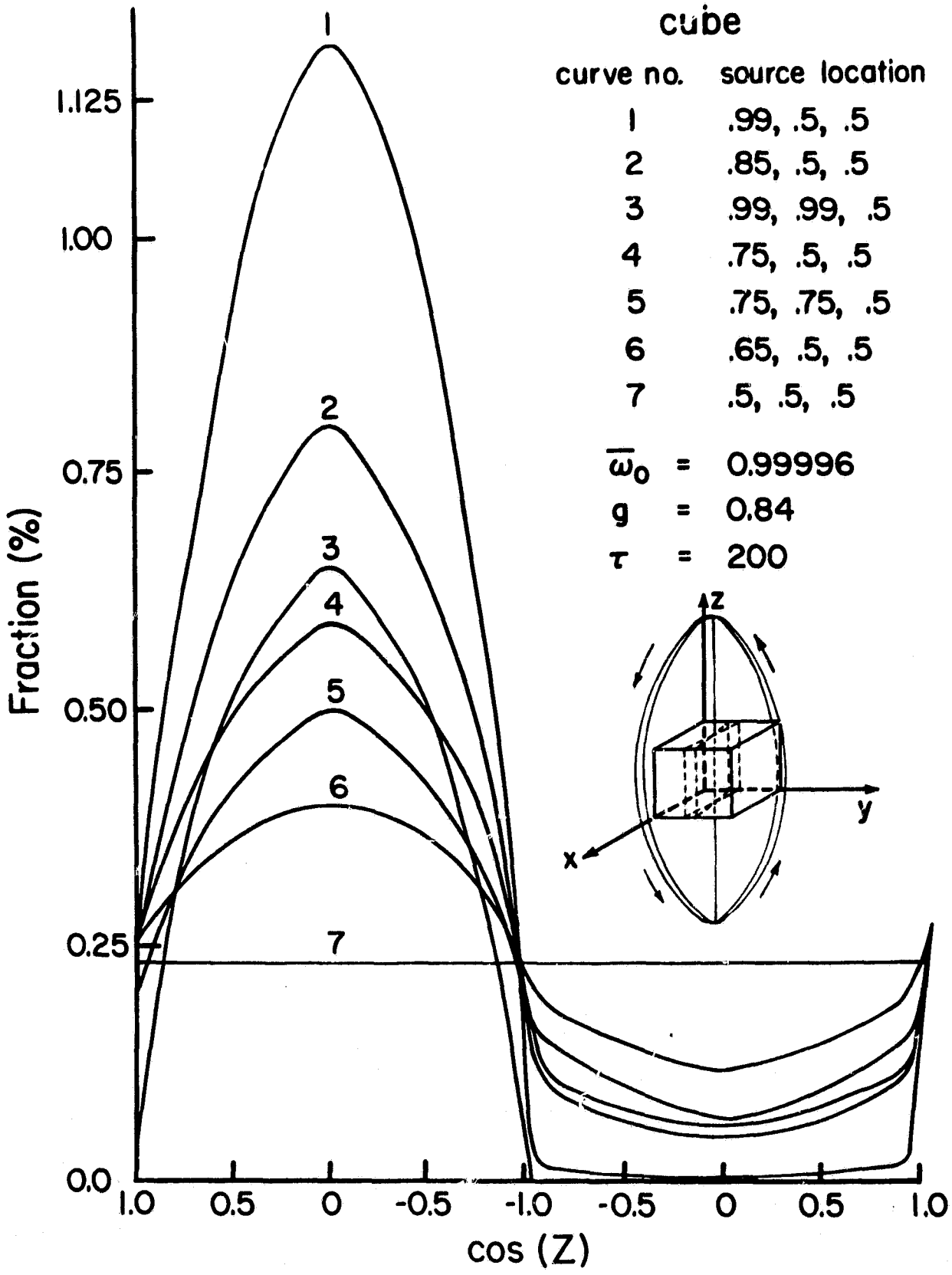
cube
curve no. source location
1 .99, .5, .5
2 .85, .5, .5
3 .99, .99, .5
4 .75, .5, .5
5 .75, .75, .5
6 .65, .5, .5
7 .5, .5, .5
$\overline{\omega}_0$ = 0.99996
g = 0.84
τ = 200
Fraction (%)
1.125
1.00
0.75
0.50
0.25
0.0
1.0
0.5
0
-0.5
-1.0
-0.5
0
0.5
1.0
cos (Z)
Z
y
x

Fig. 18

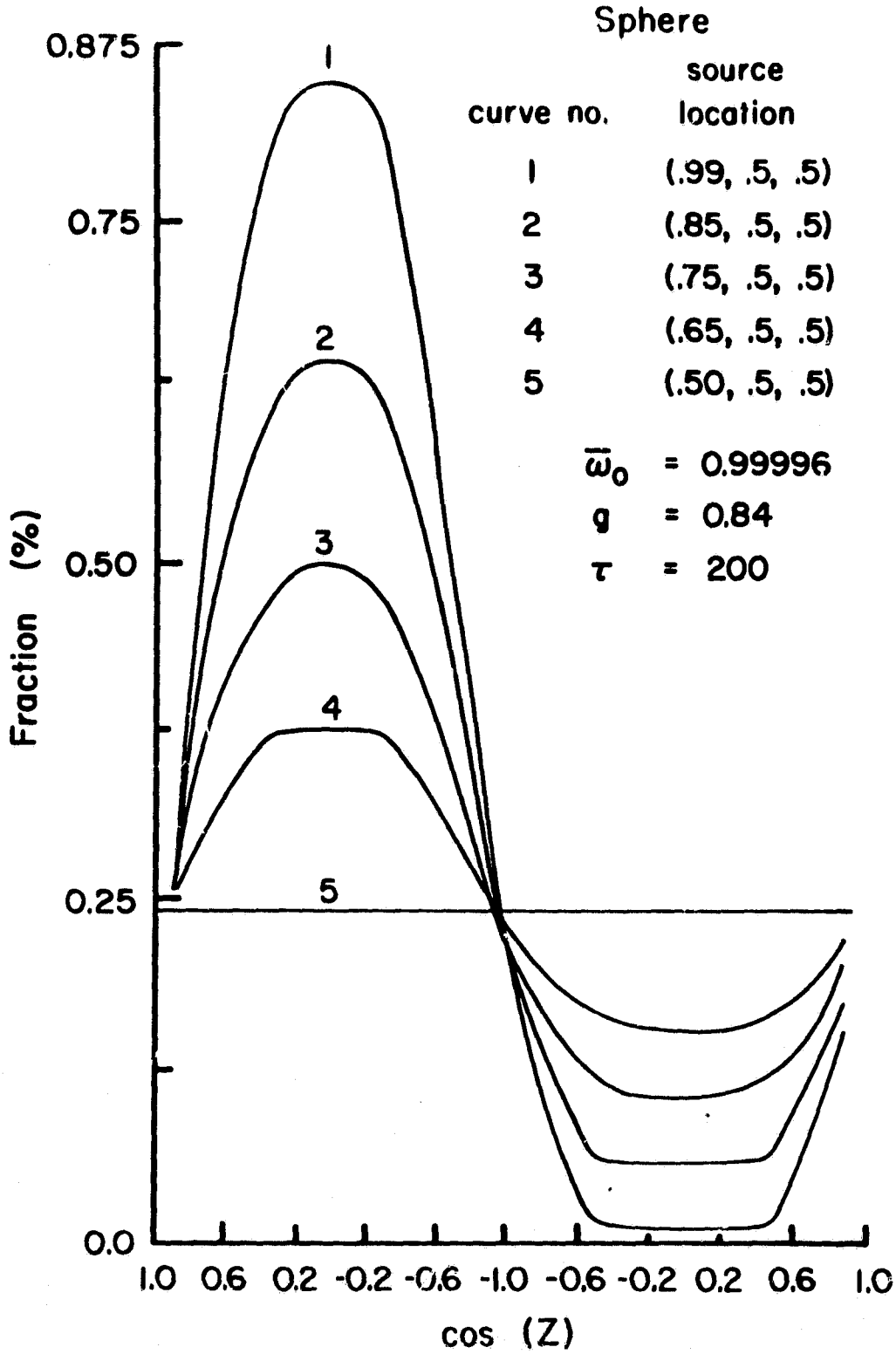
Sphere
source
curve no. location
1 (.99, .5, .5)
2 (.85, .5, .5)
3 (.75, .5, .5)
4 (.65, .5, .5)
5 (.50, .5, .5)
$\bar{\omega}_0$ = 0.99996
g = 0.84
τ = 200
Fraction (%)
0.875
0.75
0.50
0.25
0.0
1.0 0.6 0.2 -0.2 -0.6 -1.0 -0.6 -0.2 0.2 0.6 1.0
cos (Z)

Fig. 19

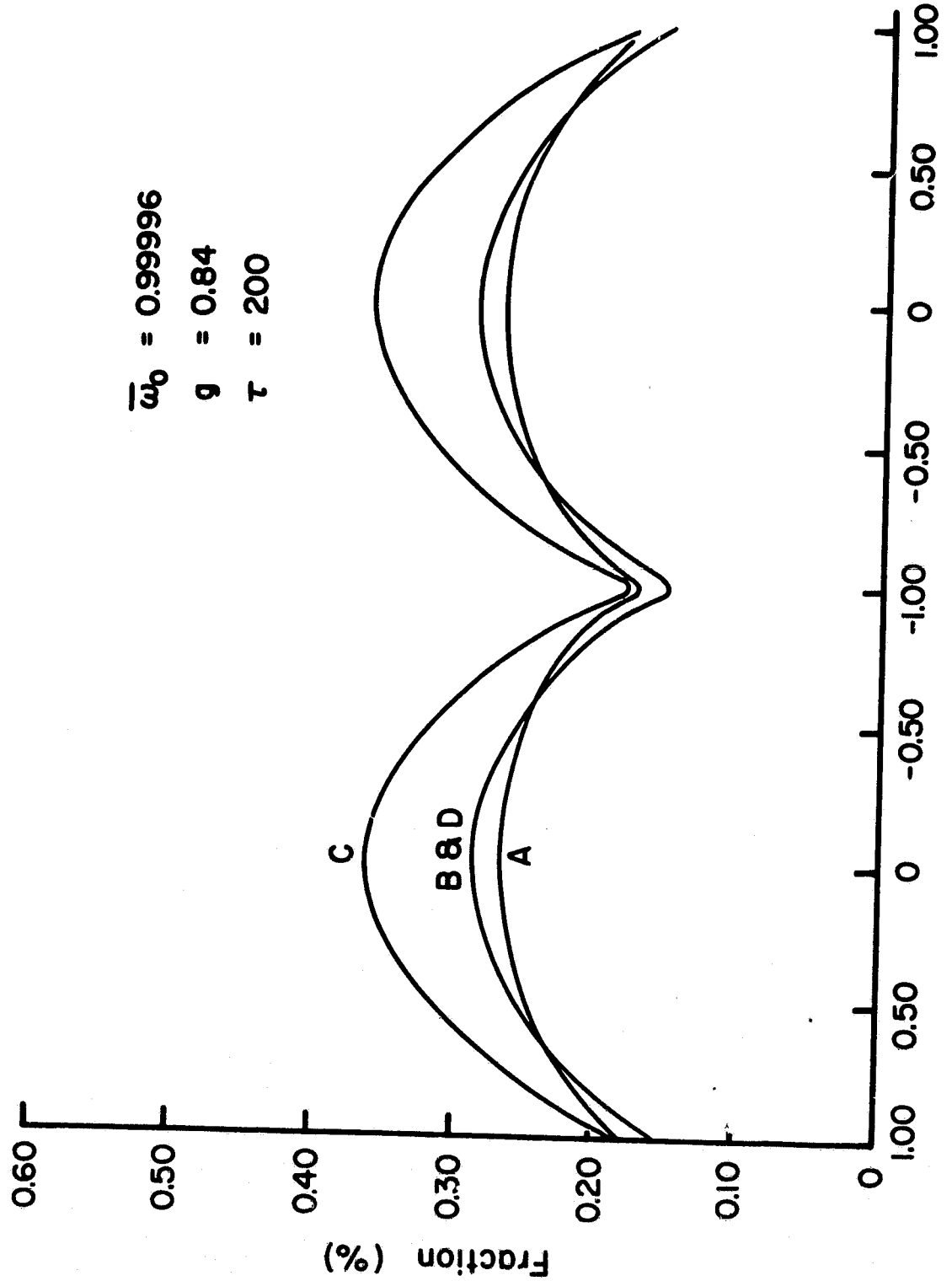
$\bar{\omega}_0$ = 0.99996
g = 0.84
τ = 200
C
B&D
A
Fraction (%)
0.60
0.50
0.40
0.30
0.20
0.10
0
1.00
0.50
0
-0.50
-1.00
cos (Z)

Fig. 20